Mantle-driven north–south dichotomy in geomagnetic polar minima

Maxime Lézin, Hagay Amit, Filipe Terra-Nova, Ingo Wardinski

Mantle-driven north–south dichotomy in geomagnetic polar minima

Maxime Lézin [a], Hagay Amit [a,*], Filipe Terra-Nova [a], Ingo Wardinski [b]

[a] Laboratoire de Planétologie et Géosciences, CNRS UMR 6112, Nantes Université, Université d'Angers, Le Mans Université, 2 rue de la Houssinière, F-44000 Nantes, France
[b] Institut Terre et Environnement Strasbourg, Ecole et Observatoire des Sciences de La Terre, Université de Strasbourg, CNRS, Strasbourg, France

ARTICLE INFO

Keywords:
Geomagnetic field
Polar minima
Tangent cylinder
Core upwelling
Core-mantle boundary
Mantle control

ABSTRACT

The geomagnetic field on the core-mantle boundary (CMB) is characterized by weak or even reversed field in the polar regions and intense flux patches at the edges of the intersection of the inner-core tangent cylinder (TC) with the CMB. This high-latitude field morphology is in agreement with thermal wind theory inside the TC in which polar upwellings disperse magnetic field lines. Furthermore, inferences from the geomagnetic secular variation hint to the presence of a westward jet at high latitudes of the northern hemisphere, also in agreement with the TC dynamical theory, but not in the southern hemisphere. Here we study polar minima in an ensemble of geomagnetic field models that span the historical era and in a set of numerical dynamo simulations with a heterogeneous outer boundary heat flux inferred from a tomographic model of lowermost mantle seismic anomalies. We quantified the polar minima using a previously-proposed expression as well as a new measure which may better capture this phenomenon. We found that throughout the historical era the geomagnetic field is characterized by stronger polar minima and more reversed flux inside the northern TC than inside the southern TC. Likewise, almost all dynamo models exhibit on average stronger polar minima in the northern hemisphere. This north/south dichotomy is explained in terms of the pattern of lowermost mantle seismic anomalies, in particular the southern centers of the two Large Low Shear-wave Velocity Provinces below Africa and the Pacific. We also investigated polar minima in planets where magnetic field models at the top of the dynamo region are available. We speculate that the absence of polar minima in Mercury's field is likely due to the thick stratified layer at the top of its core, while the strong polar minima in Jupiter's field might have a different dynamical origin than the geomagnetic polar minima.

1. Introduction

The geomagnetic field is generated by convective motions of the metallic liquid inside Earth's outer core. Geomagnetic field models inverted from observations provide vital insight into the dynamics of the outer core as well as its coupling with the mantle and the inner core. For example, temporal changes in the field termed secular variation (SV) allow to infer the fluid velocity at the top of the core (e.g. Holme, 2015). In addition, the longitudes of intense high-latitude radial geomagnetic field patches on the core-mantle boundary (CMB) correlate with positive seismic shear-wave velocity anomalies in the lower mantle (Gubbins et al., 2007) suggesting that mantle-driven core fluid downwellings concentrate these intense patches. The localisation of westward drifting low-latitude patches in the Atlantic hemisphere can be explained by a hemispherical asymmetric growth of the inner core boundary (ICB) which may indicate bottom boundary control on the geodynamo (Aubert et al., 2013). The study of the geomagnetic field may also constrain the core structure and its evolution. For example, the periodicity of the geomagnetic dipole SV is consistent with stratification at the top of the core (Buffett, 2014), though the small-scale highly concentrated field (Christensen et al., 2010) suggests that this stable layer is either thin or non-existent (Olson et al., 2017; Gastine et al., 2020). In addition, an ancient increase in the intensity of the Earth's paleomagnetic field may point to the timing of the emergence of the inner core (Biggin et al., 2015).

Outer core dynamics are strongly affected by the structure of the core, in particular the size of the inner core. The tangent cylinder (TC) is a hypothetical cylinder parallel to the Earth's spin axis and tangent to the solid inner core at the equatorial plane. The TC acts as a fluid barrier (e.g. Jones, 2007). Downwellings at the edges of the TC concentrate intense geomagnetic flux patches at the latitudes where the TC intercepts the CMB (e.g. Busse, 1975), whereas upwellings inside the TC

* Corresponding author.
E-mail address: Hagay.Amit@univ-nantes.fr (H. Amit).

https://doi.org/10.1016/j.pepi.2023.107000
Received 12 October 2022; Received in revised form 16 February 2023; Accepted 16 February 2023
Available online 2 March 2023

lead to dispersion of field lines and weak or even reversed field near the poles (e.g. Olson and Aurnou, 1999). Based on thermal wind theory, the polar upwellings are coupled with anticyclonic (westward) motions below the CMB and eastward motion above the ICB. The theory of the TC and polar minima is described in more details in Section 2.

Observations of the geomagnetic field at Earth's surface and by dedicated satellite missions (CHAMP, Swarm, etc.) are used to construct global geomagnetic field models in terms of spherical harmonics. Assuming that the mantle is a perfect insulator, these models can be downward projected to the CMB. These observations-based models show that the geomagnetic field on the CMB is dominated by an axial dipole component with the northern/southern hemisphere presenting mostly negative/positive radial field, respectively. However, since the advent of geomagnetic intensity measurements, the axial dipole is rapidly decreasing (Finlay, 2008). The dipole decrease mostly originates in the southern hemisphere (Olson and Amit, 2006), but the role of the field inside the TC in the dipole decrease is not clear.

Analysis of the geomagnetic field models may provide insight into the core dynamics. Gubbins and Bloxham (1987) analyzed a geomagnetic field model over the historical era from 1695 to 1980. Their study highlighted intense equatorially symmetric flux patches near the TC rim and polar minima inside the TC. Polar minima are manifested by weak or even reversed flux at the CMB. Gubbins and Bloxham (1987) related these field features to TC dynamics. Several studies based on geomagnetic field models noted that the polar minima are more persistent in the northern hemisphere than in the southern (e.g. Gubbins and Bloxham, 1987; Olson and Aurnou, 1999).

Core dynamics may be further gleaned by attempts to find the fluid motions below the CMB that reproduce observed temporal changes in the field, i.e. the SV. Olson and Aurnou (1999) considered a reduced model to explain the geomagnetic SV. Their flow model was assumed to be axisymmetric and focused locally on the northern area inside the TC in order to constrain large-scale TC dynamics. They inferred a polar anticyclonic vortex in the northern hemisphere. Using the thermal wind theory, they related this vortex to a polar upwelling plume that is responsible for the geomagnetic northern polar minimum. They argued that the westward vortex was persistent for at least 120 years, although its amplitude has been fluctuating with time. A similar vortex was not found inside the southern TC. Olson and Aurnou (1999) attributed this absence to either a poorer data coverage for earlier epochs in the southern hemisphere or a genuine difference between the dynamics in the two polar regions.

Classical inversions of global geomagnetic SV provide global core flow models (e.g. Holme, 2015). Hulot et al. (2002) used high quality Magsat and Oersted satellite data to construct a small-scale model of the geomagnetic SV which they inverted for the global flow at the top of the core. They found westward zonal flow inside the TC, slightly stronger in the northern hemisphere than in the southern. Similar westward zonal flow in the polar regions was reported in other global SV inversions using different datasets, methodologies and assumptions (e.g. Pais and Hulot, 2000; Amit and Olson, 2006; Holme and Olsen, 2006). As mentioned above, these westward polar vortices are consistent with polar upwellings via the thermal wind theory.

Livermore et al. (2017) opted for an intermediate modelling approach. As in Olson and Aurnou (1999), their flow model is also purely azimuthal and concentrated inside the TC, but it is not axisymmetric. They found in the northern hemisphere a strong non-axisymmetric jet at high latitudes in the Pacific hemisphere. They hypothesized that this jet could be part of an eccentric gyre that was found in global quasi-geostrophic core flow models below the CMB (e.g. Pais and Jault, 2008; Gillet et al., 2011). However, Livermore et al. (2017) did not find a similar equatorially symmetric counterpart jet in the southern hemisphere as expected under rapid rotation conditions (see Section 2). They argued that a southern high-latitude azimuthal jet is non-detectable because the radial field there is oriented almost east–west hence it is aligned with the azimuthal jet and thus the latter generates no SV.

Far more detailed insight into core dynamics in general and polar minima in particular can be obtained from 3D numerical dynamo models where the magnetic field, flow and buoyancy are all given inside the entire spherical shell. Christensen et al. (1998) ran numerical dynamos and compared their output with geomagnetic field models. They recovered high-latitude intense flux patches near the TC edge which are maintained by fluid downwellings associated with axial columnar flow. Inside the TC, they found polar minima linked to upwelling plumes. Sreenivasan and Jones (2005) found in their dynamo models that the polar minima deviate from the geographical poles at around 80° at each hemisphere and these features also exhibit a strong variability in longitude with time. In addition, they found that the magnetic field enhances the westward polar vortices which are dynamically coupled to the meridional circulation that sustains the magnetic polar minima. In the models of Sreenivasan and Jones (2005), one large upwelling plume fills the TC. Olson et al. (2017) ran numerical dynamos with a variable thickness of a stratified layer just under the outer boundary and a heterogeneous outer boundary heat flux. For a relatively thin stratified layer, polar minima are present in their dynamo models. When the layer is thicker, the polar minima disappear. Assuming that polar minima are a necessary Earth-like morphological feature of the geomagnetic field, Olson et al. (2017) concluded that a stratified layer is either thin or non-existent. In these models, the top of the spherical shell is partially stratified due to the heterogeneous outer boundary heat flux, i.e. thermal convection is subcritical/supercritical below hot/cold lower mantle, respectively (Olson et al., 2017; Mound et al., 2019). Such partial stratification may reconcile seismic evidence for stratification (e.g. Kaneshima and Matsuzawa, 2015) and geomagnetic evidence against stratification (Amit, 2014; Gastine et al., 2020).

Cao et al. (2018) used a present-day snapshot of a geomagnetic field model on the CMB to quantify the amplitude of the polar minima, which they defined as the difference between the polar radial field and the peak zonal radial field normalized by the latter (see Section 3.2). They reported values of 1 and 0.6 for the north/south polar minima ratio, respectively. In order to isolate the contribution of a steady axisymmetric flow to the polar minima, they built reduced dynamical models. They considered an axisymmetric force balance with thermal forcing for the momentum equation and an axisymmetric magnetic induction equation. Because a dynamo requires 3D motions (Cowling, 1934), they imposed a magnetic field on the outer boundary. Cao et al. (2018) established relations between the amplitudes of polar upwellings and the anticyclones inside the TC, as well as between the amplitudes of polar upwellings and the resulting magnetic polar minima. Kinematic (i.e without Lorentz force) and dynamic 2D models produced polar minima amplitudes of only ~ 0.1 with an Ekman number of 10^{-4}. When the Ekman number was decreased towards Earth's outer core values, the intensity of the polar minima became much smaller. They scaled the intensity of the polar minima with the magnetic Reynolds number and the Ekman number. According to their scaling laws indeed faster rotation gives less intense polar minima. Then, they extrapolated their results to Earth-like conditions. Estimating Earth-like thermal forcing and anticyclone speed, their extrapolations predict that a steady axisymmetric vortex would give polar minima amplitudes of $\sim 0.015-0.03$, far smaller than their observed values of $0.6-1$. 3D numerical dynamo models confirm the Ekman number dependence. From these results, they concluded that a steady axisymmetric circulation is not sufficient to produce the observed polar minima. They thus provided three alternative scenarios to depart from the simple steady axisymmetric polar vortex model. In the first scenario, Cao et al. (2018) proposed that the TC is filled by strong, small-scale helical convective turbulent rolls in addition to the large-scale polar vortex. In the second scenario, they considered a large-scale non-axisymmetric and/or time-varying polar upwelling. To generate polar minima, this non-axisymmetric upwelling has to dominate non-axisymmetric downwellings. Considering time-

varying plumes, they proposed that strong polar minima appear occasionally. In the third scenario, they proposed that a large-scale instability of the TC shear layer could generate magnetic polar minima.

Following Cao et al. (2018), we propose to infer the TC dynamics, in particular the production of polar minima, with far more extended geomagnetic observations and with a different type of dynamical simulations. For the observations, 100 COV-OBS.x1 realizations (Gillet et al., 2015) that cover the historical era are quantitatively analyzed in order to obtain statistics of polar minima as a function of time including model uncertainties. Then, we explore the numerical dynamo models of Terra-Nova et al. (2019) which contain outer boundary heat flux heterogeneity inferred from a model of seismic anomalies at the lower mantle (Masters et al., 2000). A special attention is given to hemispheric differences which may point to mantle control on TC dynamics. Next, we compare the polar minima in the geomagnetic observations and the dynamo simulations. Finally, we explore polar minima in recent magnetic field models of Mercury and Jupiter.

2. Theory

2.1. Thermal wind

The tangent cylinder is a hypothetical cylinder parallel to the Earth's spin axis and tangent to the solid inner core at the equatorial plane. The TC acts as a fluid barrier (e.g. Jones, 2007). Downwellings of outer core fluid at the edges of the TC concentrate field lines and induce intense flux patches on the CMB. To fulfill conservation of mass, these downwellings are compensated by upwellings at the poles below the CMB. Associated toroidal motions can be derived by considering approximations of the Navier–Stokes equation, i.e. the conservation of momentum. In the outer core the Ekman number, which describes the ratio of viscous to Coriolis forces is $\sim 10^{-14}$, and the Rossby number, which characterizes the ratio of inertial to Coriolis forces is $\sim 10^{-6}$ (Cormier et al., 2021). The Lorentz force may be comparable or secondary to the Coriolis force, depending on the definition of their ratio (Soderlund et al., 2012). Numerical dynamo simulations suggest that the Lorentz force is secondary (Schwaiger et al., 2019). Thus, these very low values of the Ekman and Rossby numbers suggest that the dominant horizontal force balance is between the pressure gradient and Coriolis forces, which gives the geostrophic approximation (Pedlosky, 1987):

$$2\Omega\widehat{z}\times\mathbf{u} = -\frac{1}{\rho_0}\nabla P, \tag{1}$$

where Ω is the angular velocity, $\widehat{z}$ is the unit vector in the direction of the rotation axis, $\mathbf{u}$ is the velocity vector, ρ_0 is the hydrostatic density and P is the pressure.

Due to the difference in the orientation of gravity with respect to the rotation axis of the Earth, fluid motions inside and outside the TC are distinctive (Chandrasekhar, 2013). Outside the TC on approach to the equatorial plane, gravity is nearly perpendicular to the rotation axis and the horizontal force balance indeed obeys the geostrophic approximation (1). The curl of this approximation gives the Taylor-Proudman theorem (Taylor, 1917):

$$\frac{\partial\mathbf{u}}{\partial z} = 0, \tag{2}$$

where z is the axial cylindrical coordinate. Accordingly, the flow is organized in cylindrical columns of fluid that are parallel to the rotation axis and intercept the CMB at the edge of the TC (Busse, 1975). This flow is circulating perpendicular to the rotation axis. Such motions are thus efficient in transferring heat from the ICB to the CMB in the outwards cylindrical radial direction.

Inside the TC on approach to the geographical poles, gravity is almost parallel to the rotation axis. There, columnar flow cannot transfer heat radially, hence the buoyancy force cannot be ignored:

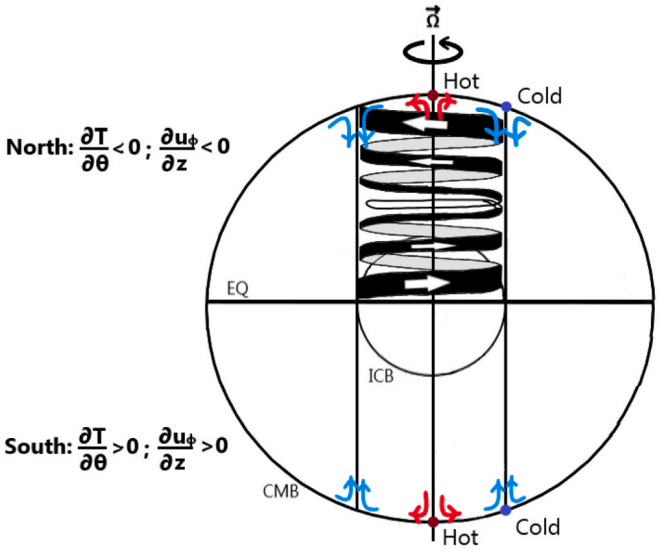

Fig. 1. Schematic illustration of TC dynamics. The polar vortex is represented by the black (front)/grey (back) ribbon and white arrows denote the circulation direction of the fluid. The thicknesses of the black/grey ribbon and the white arrows represent flow magnitude. Downwellings at the edges of the TC and upwellings at the poles are denoted by blue/red arrows, respectively. Blue/red dots at the CMB denote cold/hot fluid below the edges of the TC and the poles, respectively. The same process occurs in the southern hemisphere (not shown). Qualitative description of the thermal wind (4) in each hemisphere is given by the expressions on the left.

$$2\Omega\widehat{z}\times\mathbf{u} = -\frac{1}{\rho_0}\nabla P + \alpha g_0 T\widehat{r}, \tag{3}$$

where α is the thermal expansivity, g_0 is the gravitational acceleration on the CMB, $\widehat{r}$ is the unit vector in the radial direction and T is the temperature (or buoyancy). The curl of (3) gives the thermal wind equation (e.g. Pedlosky, 1987; Glatzmaier and Roberts, 1996). Its azimuthal component is:

$$\frac{\partial u_\phi}{\partial z} = \frac{\alpha g_0}{2\Omega R_{cmb}}\frac{\partial T}{\partial\theta}, \tag{4}$$

where u_ϕ is the azimuthal velocity, R_{cmb} is the radius of the CMB and θ is the co-latitude. Since polar upwellings (red arrows in Fig. 1) bring hotter fluid to the poles below the CMB (red dots in Fig. 1) and and downwellings (blue arrows in Fig. 1) correspond to colder fluid below the CMB at the edges of the TC (blue dots in Fig. 1), negative/positive meridional temperature gradient appears in the northern/southern TC, respectively. According to (4), these temperature gradients drive the azimuthal flow inside the TC to decrease from westward at the CMB to eastward at the ICB in both hemispheres (black/grey ribbon in Fig. 1). Indeed, seismic observations of the superrotation of the inner core with respect to the mantle (Song and Richards, 1996) are consistent with eastward flow above the ICB. The polar upwellings at the CMB disperse magnetic field lines, hence inducing polar minima. These TC dynamics were observed in laboratory experiments (Aurnou et al., 2003) and numerical dynamo simulations (e.g. Olson et al., 1999).

2.2. Axial dipole spatial sources

Because the geomagnetic field is dominated by an axial dipole (e.g. Jackson et al., 2000), and because the geomagnetic axial dipole has been rapidly decreasing (e.g. Finlay, 2008), it is important to assess the TC impact on the axial dipole and its SV. The axial dipole can be defined by the following integral on the CMB (Gubbins, 1987; Gubbins et al., 2006; Olson and Amit, 2006):

$$m_z = \frac{3R_{cmb}}{2\mu_0}\int_S B_r cos\theta dS, \tag{5}$$

where S is the CMB surface, μ_0 is the free space magnetic permeability, B_r is the radial component of the geomagnetic field and $dS = R_{cmb}^2\ sin\theta\ d\theta\ d\phi$ is the surface increment with ϕ the longitude.

Obviously, the integrand $B_r cos\theta$ at a given location contains non-dipole contributions. However, because (5) is an integral equation, its integrand $B_r cos\theta$ represents axial dipole spatial sources and sinks. This interpretation has led to important insights about the dynamical origin of the geomagnetic axial dipole and its SV. First, because the present-day axial dipole is negative, normal flux provides negative (i.e. reinforcing) local contributions to m_z, whereas reversed flux provides positive (i.e. opposite) contributions (Gubbins, 1987; Gubbins et al., 2006; Olson and Amit, 2006). Second, another integral equation was derived for the SV of the dipole (Moffatt, 1978). Based on this equation, poleward motion of normal flux and equatorward motion of reversed flux (in both hemispheres) constitute axial dipole advective sources, and conversely, equatorward motion of normal flux and poleward motion of reversed flux correspond to axial dipole advective sinks (Olson and Amit, 2006; Finlay et al., 2016). Analogous expressions for the sources and sinks of other dipole components, most notably the equatorial dipole and the associated dipole tilt, were also derived (Amit and Olson, 2008). Finally, regional contributions to the axial dipole can be obtained by regional integrations of (5). Again, each regional integration contains non-dipole contributions, but because their sum gives the axial dipole, each part can be interpreted as axial dipole sources or sinks. Such regional integrations revealed that the geomagnetic axial dipole decrease originates in the southern hemisphere (Olson and Amit, 2006) and in reversed flux patches (Terra-Nova et al., 2015; Metman et al., 2018). In Section 3.3 we propose new regional integrations of (5) in order to reveal the role of the TC in magnetic axial dipole changes.

3. Methods

3.1. Numerical dynamo simulations

We analyzed the numerical dynamo models with heterogeneous outer boundary heat flux from the set of Terra-Nova et al. (2019). Four internal control parameters characterize the models. The Ekman number describes the ratio between viscous to Coriolis forces:

$$E = \frac{\nu}{\Omega D^2}, \tag{6}$$

where ν is the kinematic viscosity and D is the shell thickness. The Rayleigh number represents convection versus retarding forces:

$$Ra = \frac{\alpha g_0 q_0 D^4}{\kappa \nu k}, \tag{7}$$

where q_0 is the mean outer boundary heat flux, κ is the thermal diffusivity and k is the thermal conductivity. The Prandtl number is the ratio of viscosity to thermal diffusivity:

$$Pr = \frac{\nu}{\kappa}. \tag{8}$$

The magnetic Prandtl number is the ratio of viscosity to magnetic diffusivity:

$$Pm = \frac{\nu}{\eta}, \tag{9}$$

where η is the magnetic diffusivity.

Thermo-chemical convection was simulated in the co-density framework in which thermal and chemical buoyancy sources are combined into one variable (e.g. Aubert et al., 2008). A heterogeneous pattern of heat flux on the outer boundary was prescribed based on a tomographic model of seismic shear-wave velocity anomalies at the lowermost mantle (Masters et al., 2000). The amplitude of the imposed heat flux heterogeneity q^* is quantified by (Olson and Christensen, 2002):

$$q^* = \frac{q_{max} - q_{min}}{2q_0}, \tag{10}$$

where q_{max} and q_{min} are the maximum and minimum heat flux, respectively. Fixed codensity was imposed on the inner boundary. Rigid and insulating conditions on both boundaries were applied for the velocity and magnetic field, respectively. The shell thickness corresponds to the size of Earth's inner core, i.e. $R_{icb}/R_{cmb} = 0.35$.

A main output parameter of the numerical dynamos is the magnetic Reynolds number which characterizes the ratio of magnetic field generation by advection and stretching to magnetic field destruction by Ohmic dissipation:

$$Rm = \frac{\mathbf{U}D}{\eta}, \tag{11}$$

where $\mathbf{U}$ is the rms velocity in the shell. The magnetic Reynolds number defines dynamo efficiency - for a given flow geometry, above a critical Rm a dynamo prevails (e.g. Moffatt, 1978). In addition, Cao et al. (2018) found that the magnetic polar minima scale with a specific Rm associated with the anticyclone speed inside the TC.

In the dynamo models time is scaled by the viscous diffusion time D^2/ν and the magnetic field is scaled by $\sqrt{\rho\mu_0\eta\Omega}$ (e.g. Christensen and Wicht, 2015). For typical values of ρ, η and Ω the magnetic field output in the dynamo models is given in units of mT (Amit et al., 2011). The set of dynamo models span Ekman numbers in the range $3{\cdot}10^{-4}$ to $3{\cdot}10^{-5}$, Rayleigh numbers of $5{\cdot}10^5$ to $9{\cdot}10^7$, magnetic Prandtl numbers of 0.8 to 9 and amplitudes of heat flux heterogeneity of 0.4 to 1, while the Prandtl number is fixed to 1. For governing equations, control parameters, general output parameters and more details see Terra-Nova et al. (2019).

3.2. Polar minima quantification

In order to quantify the polar minima, we analyzed the radial magnetic field on the CMB. Following Cao et al. (2018), we first used an expression which is based on B_r averaged along latitude lines (zonal radial field) to quantify polar minima:

$$\frac{|dB_r^z|}{max|B_r^z|} = \begin{cases} \dfrac{|B_r^{NP} - min(B_r^z)|}{max|B_r^z|} & for\ the\ northern\ hemisphere \\ \dfrac{|B_r^{SP} - max(B_r^z)|}{max|B_r^z|} & for\ the\ southern\ hemisphere, \end{cases} \tag{12}$$

where B_r^{NP} and B_r^{SP} are the values of the radial field at the northern and southern pole, respectively, $min(B_r^z)$ is the minimum zonal radial field, i.e. the most intense zonal radial field in the northern hemisphere, and $max(B_r^z)$ is the most intense zonal radial field in the southern hemisphere. The difference between the polar and peak values is normalized by $max|B_r^z|$ which is the most intense zonal radial field over both hemispheres.

Because the ratio (12) relies on the zonal radial field, it conceals the magnetic field longitudinal variations and therefore strongly smooths the estimate of peak field magnitude outside the TC. In order to adequately quantify the polar minima, a proper measure of the peak field should be used to calculate the difference with respect to the polar value. To overcome this problem, we propose a new measure for polar minima considering the most intense value of B_r (not its zonal value) for each hemisphere:

Table 1

Polar minima statistics in the numerical dynamo models. $\frac{|dB_r^z|}{max|B_r^z|}$ is the polar minima based on (12), $\frac{|dB_r|}{max|B_r^z|}$ is the polar minima based on (13). $\frac{S_{TC}^{rev}}{S_{TC}}$ is the relative area of reversed flux inside the TC (14). λ_{cm} and ϕ_{cm} are the latitude and longitude of the center of mass of reversed flux inside the TC (18). The standard deviations represent here the temporal variability. Earth values are time averages over the historical period according to the COV-OBS.x1 model. Mercury and Jupiter polar minima are based on the models of Wardinski et al. (2021) and Sharan et al. (2022), respectively. Other values for Mercury and Jupiter are not given due to uncertainties in their internal structures, in particular the sizes of their TCs. Case numbers correspond to those in Terra-Nova et al. (2019).

Case	$\frac{\lvert dB_r^z\rvert}{max\lvert B_r^z\rvert}$		$\frac{\lvert dB_r\rvert}{max\lvert B_r^z\rvert}$		$\frac{S_{TC}^{rev}}{S_{TC}}$		λ_{cm} (°)		ϕ_{cm} (°)	
	North	South	North	South	North	South	North	South	North	South
Earth	0.80	0.35	2.19	1.16	0.19	0.07	78.96	−76.80	−25.74	39.29
	±0.09	±0.09	±0.17	±0.18	±0.04	±0.03	±1.92	±1.31	±34.58	±9.70
Mercury	0	0.03	0.01	0.05	–	–	–	–	–	–
Jupiter	0.21	0	3.09	1.57	–	–	–	–	–	–
2	0.67	0.46	3.05	2.18	0.02	0.01	79.39	−81.68	4.17	−30.85
	±0.26	±0.28	±0.98	±0.92	±0.04	±0.03	±5.13	±5.53	±116.40	±103.02
3	0.82	0.61	3.43	2.91	0.11	0.08	78.86	−80.31	1.09	−12.19
	±0.31	±0.33	±1.07	±0.96	±0.09	±0.08	±4.53	±5.67	±105.93	±104.75
4	0.83	0.65	3.75	3.07	0.12	0.07	78.79	−81.10	−5.42	−11.04
	±0.31	±0.31	±0.97	±0.97	±0.09	±0.07	±4.18	±5.45	±114.99	±116.53
5	0.88	0.72	3.86	3.14	0.23	0.17	77.74	−80.75	−6.21	−9.12
	±0.35	±0.37	±1.12	±1.07	±0.12	±0.11	±3.23	±4.84	±110.01	±110.15
6	1.06	0.70	3.27	2.96	0.18	0.11	80.70	−80.70	−14.46	27.87
	±0.29	±0.39	±0.90	±1.13	±0.10	±0.09	±3.64	±5.39	±103.83	±97.66
7	1.08	0.77	3.50	3.31	0.27	0.17	79.28	−81.56	−5.86	11.86
	±0.36	±0.38	±0.91	±1.12	±0.11	±0.11	±2.76	±4.59	±109.13	±99.48
8	1.09	0.70	3.52	3.43	0.27	0.16	79.00	−80.26	−22.25	7.49
	±0.37	±0.39	±1.07	±1.32	±0.13	±0.11	±3.05	±5.05	±105.34	±107.80
9	0.83	0.11	3.60	1.22	0.11	0.07	77.50	−75.04	36.68	32.66
	±0.38	±0.15	±1.20	±0.61	±0.11	±0.06	±5.10	±3.06	±89.61	±141.02
10	1.02	0.76	4.11	3.69	0.36	0.24	77.38	−80.41	−8.19	11.15
	±0.42	±0.44	±1.43	±1.33	±0.15	±0.12	±2.61	±4.49	±106.07	±105.36
11	1.09	0.74	4.25	4.07	0.41	0.28	77.35	−80.00	−18.59	6.25
	±0.44	±0.47	±1.41	±1.65	±0.16	±0.14	±2.48	±4.27	±110.28	±108.40
12	1.03	0.72	3.58	2.82	0.27	0.18	78.37	−80.25	−2.91	12.96
	±0.42	±0.44	±1.08	±0.99	±0.15	±0.12	±3.37	±4.99	±104.13	±102.61
13	1.06	0.68	3.88	2.83	0.30	0.23	78.21	−80.12	−10.05	13.45
	±0.43	±0.43	±1.38	±1.09	±0.15	±0.13	±3.11	±4.57	±108.92	±98.78
15	0.62	0.44	2.60	2.00	0.03	0.01	80.05	−82.35	−7.90	0.00
	±0.33	±0.31	±0.93	±0.88	±0.04	±0.02	±5.42	±6.04	±112.20	±106.58
16	0.70	0.51	3.12	2.45	0.07	0.03	79.00	−80.35	0.84	6.78
	±0.36	±0.31	±0.98	±0.95	±0.07	±0.05	±4.82	±6.10	±110.00	±111.92
17	0.70	0.57	3.30	2.59	0.12	0.08	77.62	−80.18	−10.00	−0.60
	±0.38	±0.33	±1.23	±1.07	±0.10	±0.08	±4.28	±5.61	±102.08	±106.13
18	0.75	0.63	3.55	2.86	0.17	0.11	77.61	−80.23	−18.43	−8.89
	±0.39	±0.38	±1.30	±1.08	±0.11	±0.09	±3.72	±5.39	±108.64	±103.55
19	1.09	0.70	3.52	3.43	0.28	0.16	79.00	−80.26	−22.25	7.51
	±0.36	±0.39	±1.07	±1.32	±0.13	±0.11	±3.03	±5.05	±105.43	±107.87
20	0.93	0.67	2.85	2.29	0.14	0.06	80.36	−82.23	5.96	26.29
	±0.34	±0.37	±1.02	±0.89	±0.10	±0.06	±4.06	±5.36	±103.29	±99.77
21	0.97	0.66	2.82	2.91	0.16	0.07	80.43	−81.26	−27.43	17.73
	±0.33	±0.36	±0.86	±1.36	±0.11	±0.07	±3.77	±5.56	±105.71	±108.42
22	1.03	0.65	2.67	2.04	0.14	0.07	81.22	−82.11	−9.39	34.35
	±0.34	±0.35	±0.82	±1.19	±0.09	±0.07	±3.72	±5.35	±107.05	±101.83
23	1.01	0.59	2.71	2.15	0.15	0.08	80.54	−80.69	−16.19	24.27
	±0.35	±0.35	±0.70	±0.87	±0.10	±0.08	±3.91	±5.57	±105.07	±102.86
26	0.46	0.38	2.38	1.80	0.00	0.00	80.33	−82.18	14.68	13.55
	±0.26	±0.27	±0.81	±0.85	±0.01	±0.01	±5.78	±6.24	±103.22	±104.83
27	0.44	0.41	2.20	2.00	0.00	0.00	79.61	−80.90	1.31	−12.94
	±0.28	±0.25	±0.85	±0.83	±0.02	±0.01	±5.74	±6.32	±110.22	±121.14
28	0.65	0.54	3.34	2.74	0.12	0.05	77.50	−79.55	−9.47	3.99
	±0.37	±0.36	±1.29	±1.19	±0.09	±0.06	±4.24	±5.60	±106.76	±108.42

$$\frac{|dB_r|}{max|B_r^z|} = \begin{cases} \dfrac{|B_r^{NP} - min(B_r)|}{max|B_r^z|} & for\ the\ northern\ hemisphere \\ \dfrac{|B_r^{SP} - max(B_r)|}{max|B_r^z|} & for\ the\ southern\ hemisphere. \end{cases} \tag{13}$$

Note that the normalization in (13) is the same as in (12). Therefore, while the ratio (12) is basically in the range 0 −1, our proposed ratio (13) may exceed unity. We focus on the interpretation of the time dependence and hemispherical differences rather than the absolute values of the ratios. The ratio (13) relies on the strength of high-latitude geomagnetic flux patches and hence may better represent the amplitude of polar minima.

Polar minima may be related to reversed flux patches inside the TC (Gubbins and Bloxham, 1987; Olson and Aurnou, 1999; Sreenivasan and Jones, 2005). We therefore calculated the relative TC area of reversed flux:

$$\frac{S_{TC}^{rev}}{S_{TC}} = \int_{TC} dS^{rev} \Big/ \int_{TC} dS, \tag{14}$$

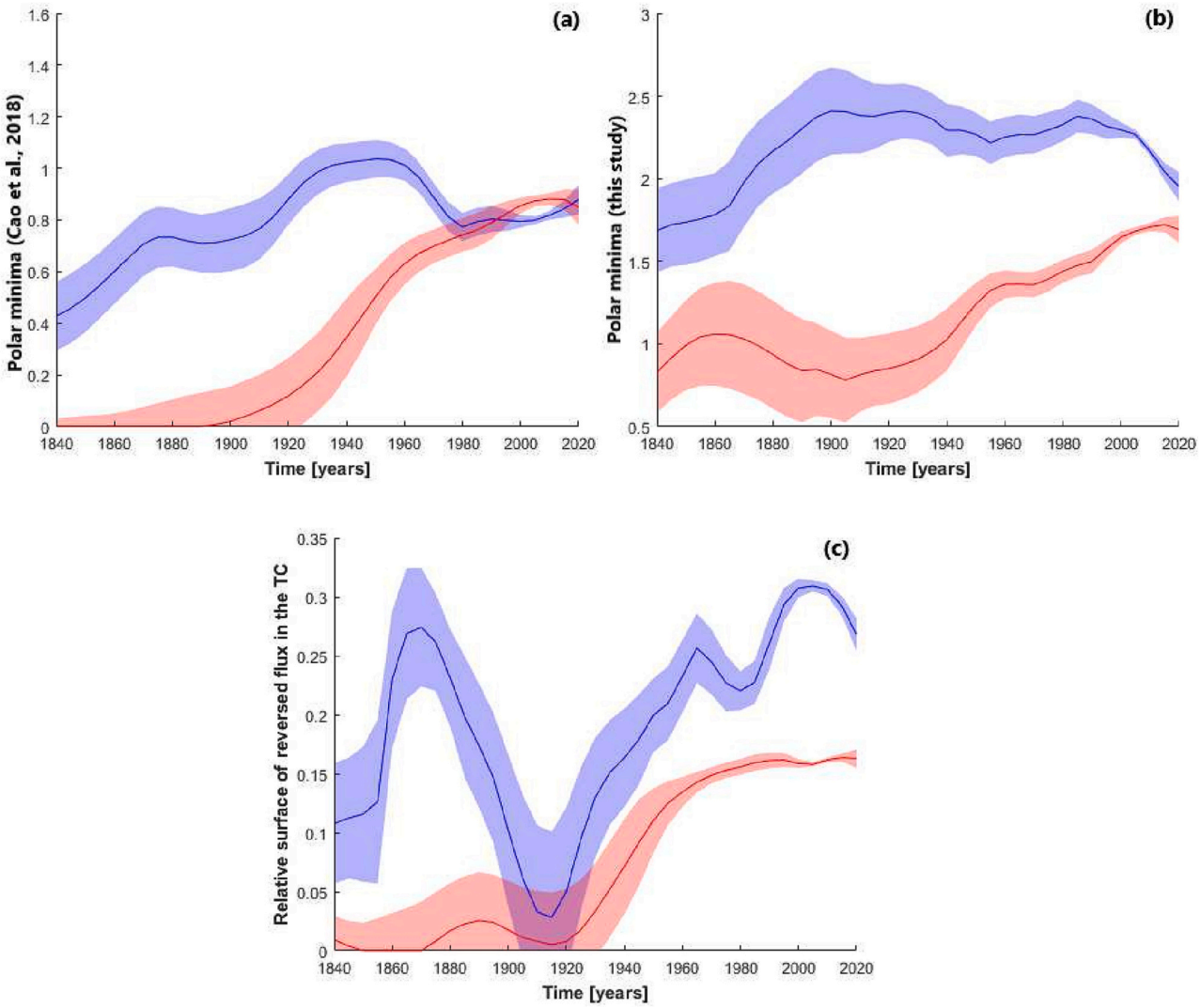

Fig. 2. Quantification of polar minima (top) and the relative surface of reversed flux inside the TC (bottom) based on the COV-OBS.x1 ensemble (Gillet et al., 2015). Blue/red denote the northern/southern hemispheres, respectively. The standard deviation (19) from 100 COV-OBS.x1 realizations are denoted by pale blue/red for northern/southern hemispheres, respectively. (a) Quantified polar minima $\frac{|dB_r^z|}{max|B_r^z|}$ based on (12). (b) Quantified polar minima $\frac{|dB_r|}{max|B_r^z|}$ based on (13). (c) Relative reversed flux surface area inside the TC (14).

where dS^{rev} is where the field is reversed, i.e. its sign is opposite to that of the axial dipole field. The integrations in (14) are over the CMB surface inside the TC at both hemispheres.

The locations of the reversed flux patches may also provide information on the dynamics in the TC. We computed the weighted mean co-latitude of reversed flux:

$$\theta_{mean} = \int_{TC} \theta B_r \, dS^{rev} \Big/ \int_{TC} B_r \, dS^{rev}, \tag{15}$$

where the weight in (15) is the radial field. Next, we computed the center of mass of reversed flux. Using spherical coordinates gives averaging errors due to longitude discontinuity from 0° to 360°. In addition, averaging the locations of two patches with equivalent latitudes but longitudes 180° apart would give the patches latitude instead of the geographical pole which would be their actual center of mass. In order to overcome these problems, we transformed the coordinates of the reversed flux regions to Cartesian coordinates:

$$\begin{aligned} x &= sin\theta cos\phi \\ y &= sin\theta sin\phi \\ z &= cos\theta. \end{aligned} \tag{16}$$

Thus, calculation of the center of mass of the x coordinate x_{cm} is:

$$x_{cm} = \int_{TC} xB_r \, dS^{rev} \Big/ \int_{TC} B_r \, dS^{rev}, \tag{17}$$

where in (17) the weight is again B_r. Similarly, we computed y_{cm} and z_{cm}. Finally, the spherical coordinates of the center of mass of reversed flux ϕ_{cm} and θ_{cm} were obtained by re-transforming x_{cm}, y_{cm} and z_{cm} to spherical coordinates:

$$\begin{aligned} \phi_{cm} &= tan^{-1}\left(y_{cm}/x_{cm}\right) \\ \theta_{cm} &= cos^{-1}\left(z_{cm}\right). \end{aligned} \tag{18}$$

Note that the center of mass may not lie on the CMB, but we nevertheless report its projection to the CMB. For convenience we reported latitudes (λ) rather than co-latitudes (θ).

All the above calculations were applied to the 100 COV-OBS.x1 realizations (Gillet et al., 2015) and to the output from the numerical dynamo simulations (Terra-Nova et al., 2019). For the COV-OBS.x1 ensemble, we analyzed the mean of the 100 realizations as well as the individual realizations. For each quantity, we calculated the values

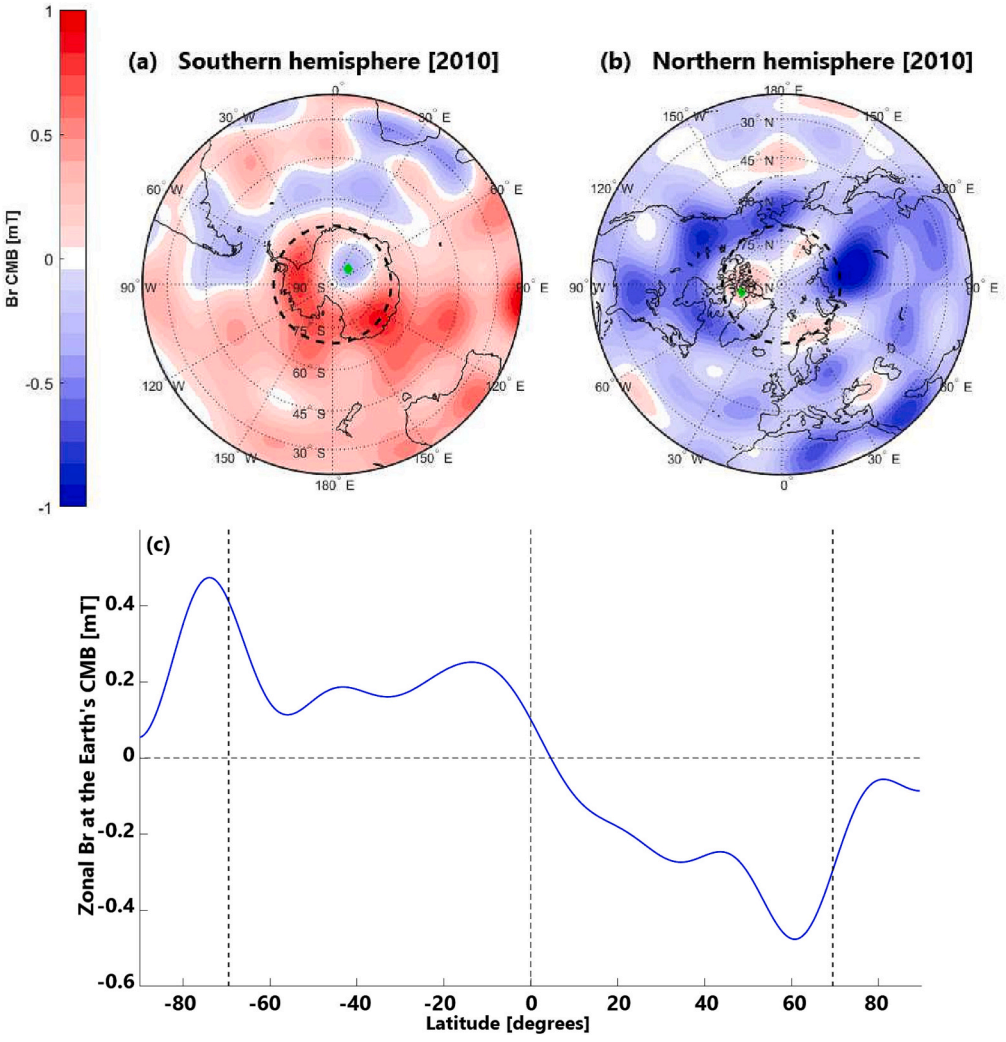

Fig. 3. South (a) and North (b) polar views of B_r at the CMB for the year 2010 from the mean of 100 COV-OBS.x1 realizations. (c) Zonal B_r vs. latitude. The TC and equator are denoted by dashed vertical lines. Polar minima values for the northern hemisphere are $\frac{|dB_r^z|}{max|B_r^z|} = 0.82$; $\frac{|dB_r|}{max|B_r^z|} = 2.17$; $\frac{S_{TC}^{rev}}{S_{TC}} = 30.60\%$; $\lambda_{mean} = 76.37°$; $\lambda_{cm} = 75.87°$; $\phi_{cm} = -78.98°$. For the southern hemisphere $\frac{|dB_r^z|}{max|B_r^z|} = 0.88$; $\frac{|dB_r|}{max|B_r^z|} = 1.71$; $\frac{S_{TC}^{rev}}{S_{TC}} = 16.17\%$; $\lambda_{mean} = -82.29°$; $\lambda_{cm} = -82.31°$; $\phi_{cm} = 46.90°$. Green diamonds in (a) and (b) correspond to the reversed flux center of mass.

based on the mean model and the standard deviation based on the 100 realizations:

$$SD = \sqrt{\left(\sum_{i=1}^{100}(V_i - \overline{V})^2\right) \Big/ 100}, \tag{19}$$

where V_i represents a value from realization i (Eqs. (12)–(18)) and $\overline{V} = \sum_{i=1}^{100} V_i/100$. For the dynamo simulations, we analyzed long timeseries of hundreds of snapshots separated by ∼1 advection time (see Terra-Nova et al., 2019). For the dynamo models, average and standard deviations are with respect to simulation time (see Table 1). Finally, we computed the correlations $C^z\left(\frac{|dB_r^z|}{max|B_r^z|}, \frac{S_{TC}^{rev}}{S_{TC}}\right)$ and $C\left(\frac{|dB_r|}{max|B_r^z|}, \frac{S_{TC}^{rev}}{S_{TC}}\right)$ between the timeseries of polar minima amplitude and the surface area of reversed flux in the TC based on the two expressions (12) and (13), respectively.

3.3. Axial dipole spatial sources and the tangent cylinder

We applied (5) to the total CMB surface as well as to four parts of it:

$$\begin{aligned} m_z^{N_{in}} &= \frac{3R_{cmb}}{2\mu_0}\int_0^{\theta_{TC}} B_r cos\theta dS \\ m_z^{S_{in}} &= \frac{3R_{cmb}}{2\mu_0}\int_{\pi-\theta_{TC}}^{\pi} B_r cos\theta dS \\ m_z^{N_{out}} &= \frac{3R_{cmb}}{2\mu_0}\int_{\theta_{TC}}^{\pi/2} B_r cos\theta dS \\ m_z^{S_{out}} &= \frac{3R_{cmb}}{2\mu_0}\int_{\pi/2}^{\pi-\theta_{TC}} B_r cos\theta dS, \end{aligned} \tag{20}$$

where $m_z^{N_{in}}$ is the outcome of (5) integrated inside the northern TC, $m_z^{S_{in}}$ is the (5) integral inside the southern TC, $m_z^{N_{out}}$ corresponds to (5) integrated in the northern hemisphere outside the TC and $m_z^{S_{out}}$ applies in the southern hemisphere outside the TC. The co-latitude of the TC is given by $sin(\theta_{TC}) = R_{icb}/R_{cmb}$.

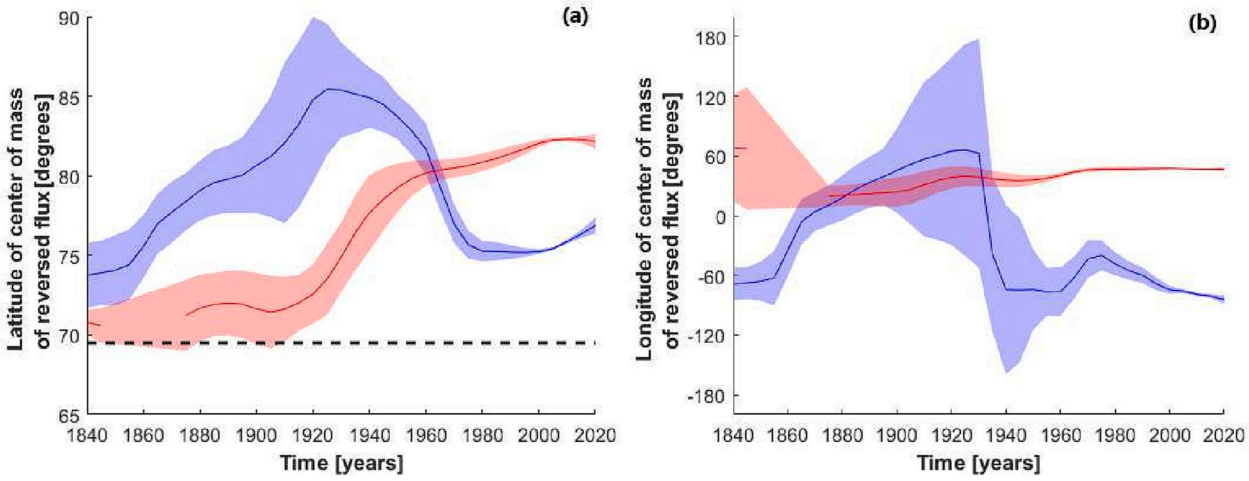

Fig. 4. Center of mass latitude (a) and longitude (b) of reversed flux inside the TC for each hemisphere. Colors as in Fig. 2. Horizontal dashed black line in (a) denotes the TC latitude. Absence of solid red line between 1845–1875 reflects no reversed flux in the southern TC at that period in the mean model, but reversed flux exists in some realizations, hence the existence of standard deviation at this period.

4. Results

4.1. Geomagnetic field models

We start with the analysis of the historical COV-OBS.x1 model (Gillet et al., 2015) derived from geomagnetic observations. Fig. 2a shows the polar minima amplitudes (12) based on Cao et al. (2018). Here we substantially extend their work by applying it to the entire historical era. The northern polar minimum amplitude increases to a peak value in 1950. Then it decreases until 1980 and remains roughly constant for the last 40 years. Overall, based on (12), a strong northern polar minimum larger than 0.5 prevails throughout almost the entire period. For the southern hemisphere, there is almost no polar minimum until 1900. Then it grows until present, with a weaker growth rate in the last 60 years. The southern polar minimum exceeds the northern between 1995 and 2015 based on (12). Recall that a change in the polar minima amplitudes does not necessarily mean that the polar field itself is changing, but that there is a relative change compared to the surrounding field.

Fig. 2b shows our proposed measure of polar minima amplitudes (13). The northern polar minimum amplitude increases to a peak value in 1900. It remains roughly constant until 1985 and decreases thereafter. For the southern hemisphere, the polar minimum is significantly weaker. Overall, for the entire historical period, based on our new measure, the northern polar minimum always exceeds the southern. In addition, the difference between the northern and southern polar minima based on (13) is larger than that based on (12). For both quantities, the standard deviation decreases from 1840 to 2020 (Fig. 2a and b).

Fig. 2c shows the time dependence of the area of reversed flux inside the TC. The northern TC contains reversed flux at all times, with its area strongly fluctuating. It increased from ∼10% in 1840 to ∼27% in 1870. Then, it dropped to less than 5% in 1915. The northern TC area increased again to ∼26% in 1965 and remained above 20% until present. In the southern hemisphere, until 1920 the mean model was almost absent of reversed flux inside the TC area, although some realizations contain reversed flux inside the southern TC for this period (see pale red

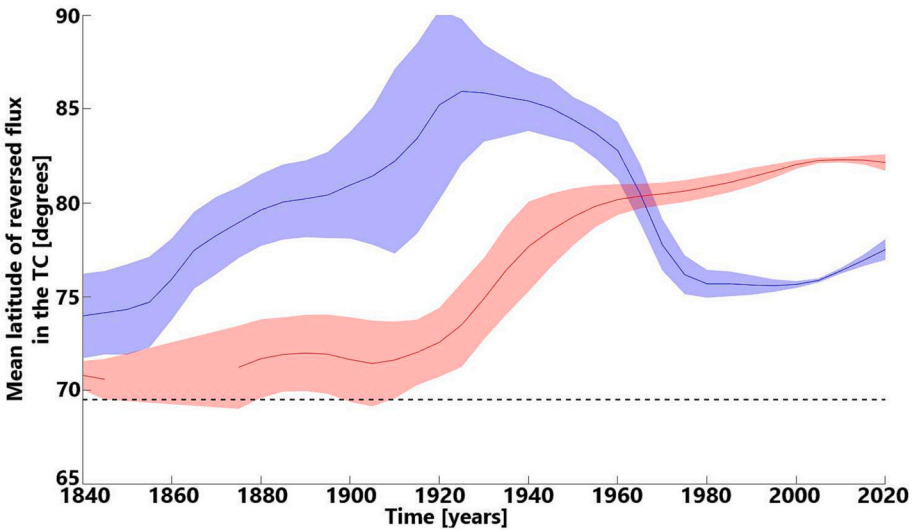

Fig. 5. Mean latitude of reversed flux inside the TC for each hemisphere. Horizontal dashed black line denotes the TC latitude.

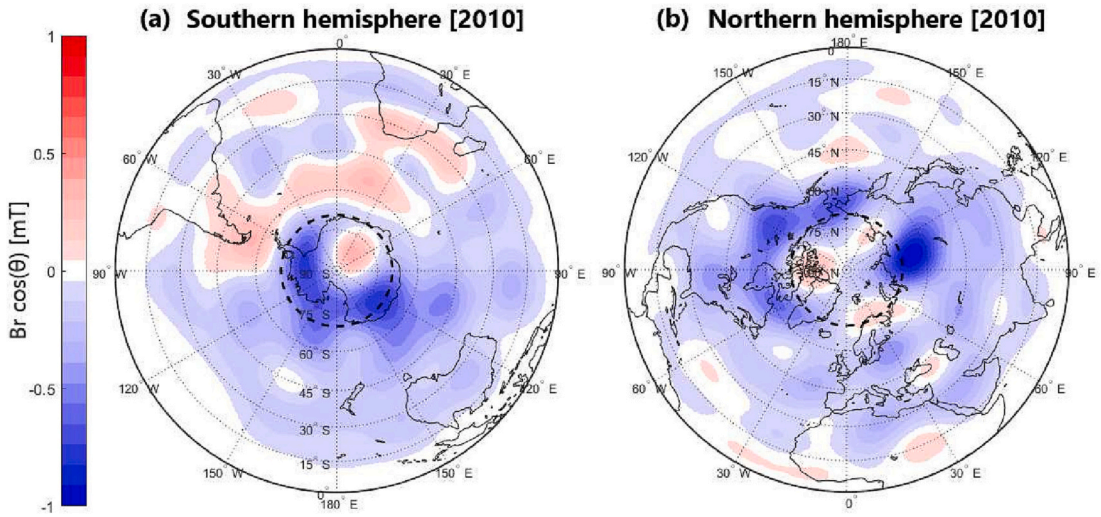

Fig. 6. Polar views of the spatial contributions to the axial dipole for the southern (a) and northern (b) hemispheres in 2010 for the mean of 100 COV-OBS.x1 realizations.

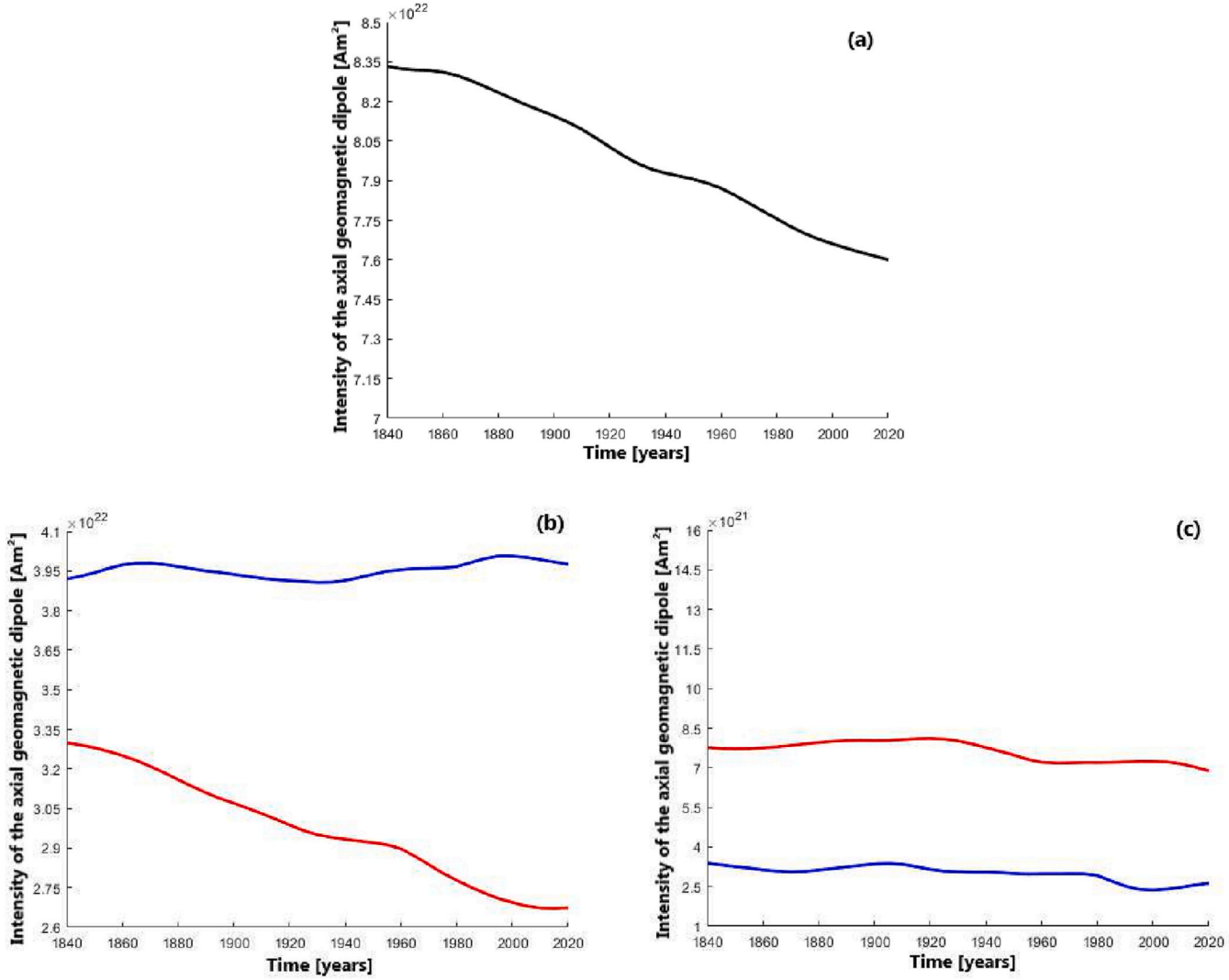

Fig. 7. Intensity (i.e. absolute value) of the axial geomagnetic dipole (in $A.m^2$) for the period 1840 to 2020 for the mean of 100 COV-OBS.x1 realizations. (a) Total intensity. (b) Contributions from outside the TC. (c) Contributions from inside the TC. In (b) and (c) northern/southern hemispheres are denoted by blue/red lines, respectively. Note the different scales but the same scale ranges in all panels which allows a direct comparison.

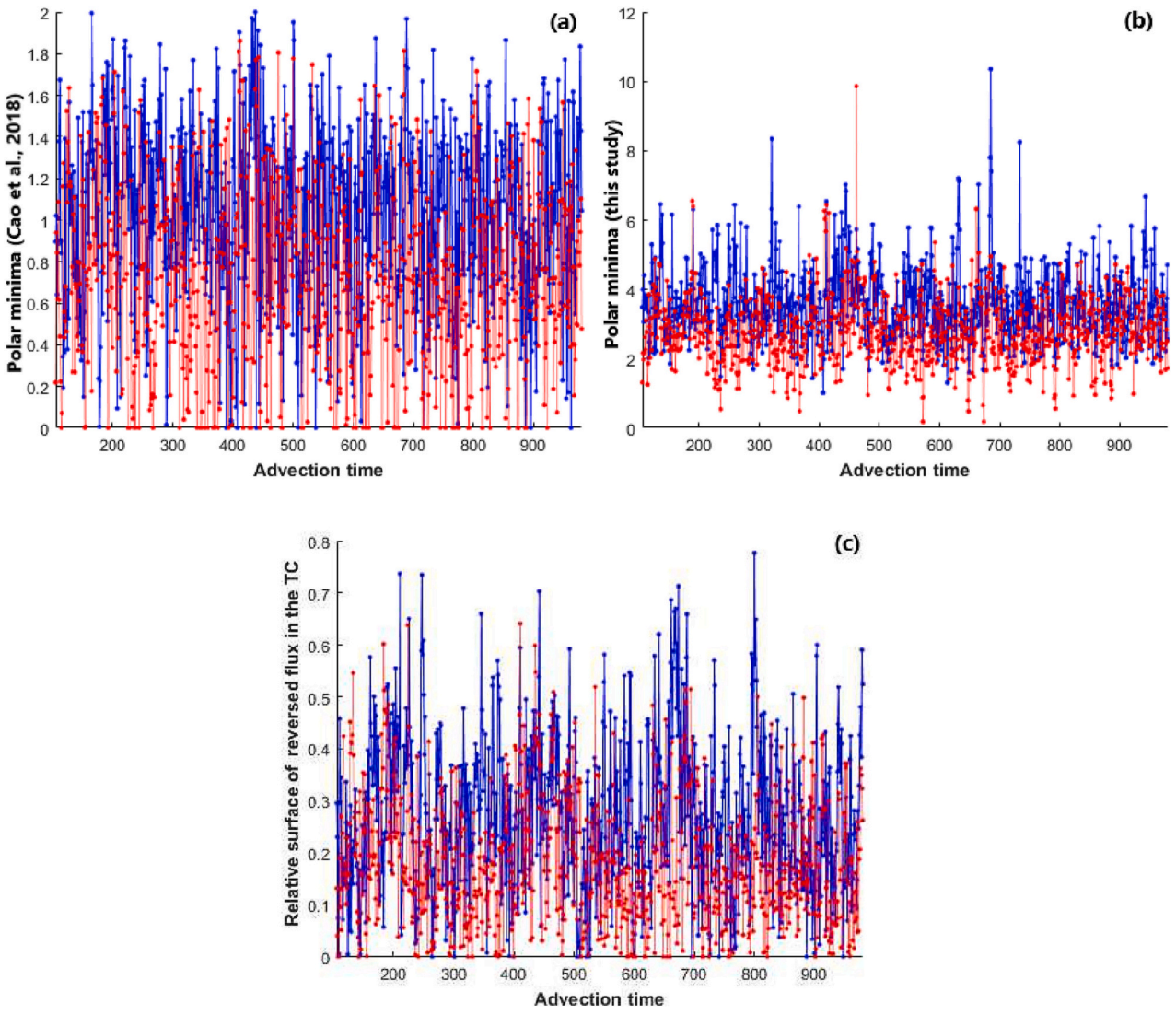

Fig. 8. Quantification of polar minima (top) and the surface of reversed flux inside the TC (bottom) for the numerical dynamo model case 12 of Terra-Nova et al. (2019). Blue/red denote northern/southern hemispheres, respectively. (a) Quantified polar minimum $\frac{|dB_r^s|}{max|B_r^s|}$(12). (b) Quantified polar minimum $\frac{|dB_r|}{max|B_r^s|}$(13). (c) Relative reversed flux surface area inside the TC (14).

in Fig. 2c). Thereafter it increased to ∼15% in 1965. After 1965, the area of the southern reversed flux remained almost constant until present. For both hemispheres, the standard deviation decreases with time. Overall, Fig. 2 provides evidence for stronger time dependence in the northern TC, especially concerning the surface of reversed flux inside the TC (Fig. 2c).

Figs. 3a and b and A1–A3a and b show polar views of the radial geomagnetic field on the CMB for four different snapshots of the mean of 100 COV-OBS.x1 realizations. The TC is denoted by the dashed black circle. The green diamonds show the centers of mass of the reversed flux inside the TC. Figs. 3c and A1–A3c show the corresponding zonal radial fields vs. latitude, with the TC represented by black dashed vertical lines.

In 2010 (Fig. 3), both polar minima (northern and southern) are relatively strong (Fig. 2a and b). The northern reversed flux covers a large area (∼ 31%) of the TC (Fig. 2c) with the reversed flux fragmented into three off-pole patches (Fig. 3b). In contrast, in the southern hemisphere the reversed flux is concentrated in a single patch close to the south pole (Fig. 3a). The magnitude of the southern polar minimum is slightly larger according to (12). However, according to (13) the northern polar minimum is more intense. For the year 1960 (Fig. A1), the northern polar minimum is stronger than in 2010 (Fig. 2) with reversed flux that covers an area of ∼ 23% of the TC (Fig. 2c). The reversed flux is localized mostly around the north pole, leading to intense polar minima (Fig. 2a and b). In the southern TC, there is also a significant area (∼ 13%) of reversed flux but off the pole (Fig. A1a). The southern polar minimum is weaker than the northern and less intense than in 2010 (Fig. 2a and b). In 1910 (Fig. A2), the northern polar minimum is also strong despite the reversed flux covering only a small area (∼ 3%) of the TC (Fig. 2c). Here the strong polar minimum in the northern hemisphere is mostly due to a weak normal flux inside the TC and large intense patches of normal flux outside the TC. In the southern TC, the area of reversed flux is also small (∼ 1%) but the normal flux inside the TC is intense. It results in a significantly weaker polar minimum in the southern hemisphere than in the northern (Fig. 2a and b). For the year 1860 (Fig. A3), the northern polar minimum is strong due to the abundant reversed flux that covers ∼ 23% of the TC area (Fig. 2c) and large patches of normal flux outside the TC. In contrast, there is no reversed flux in the southern TC, yielding practically no polar minimum

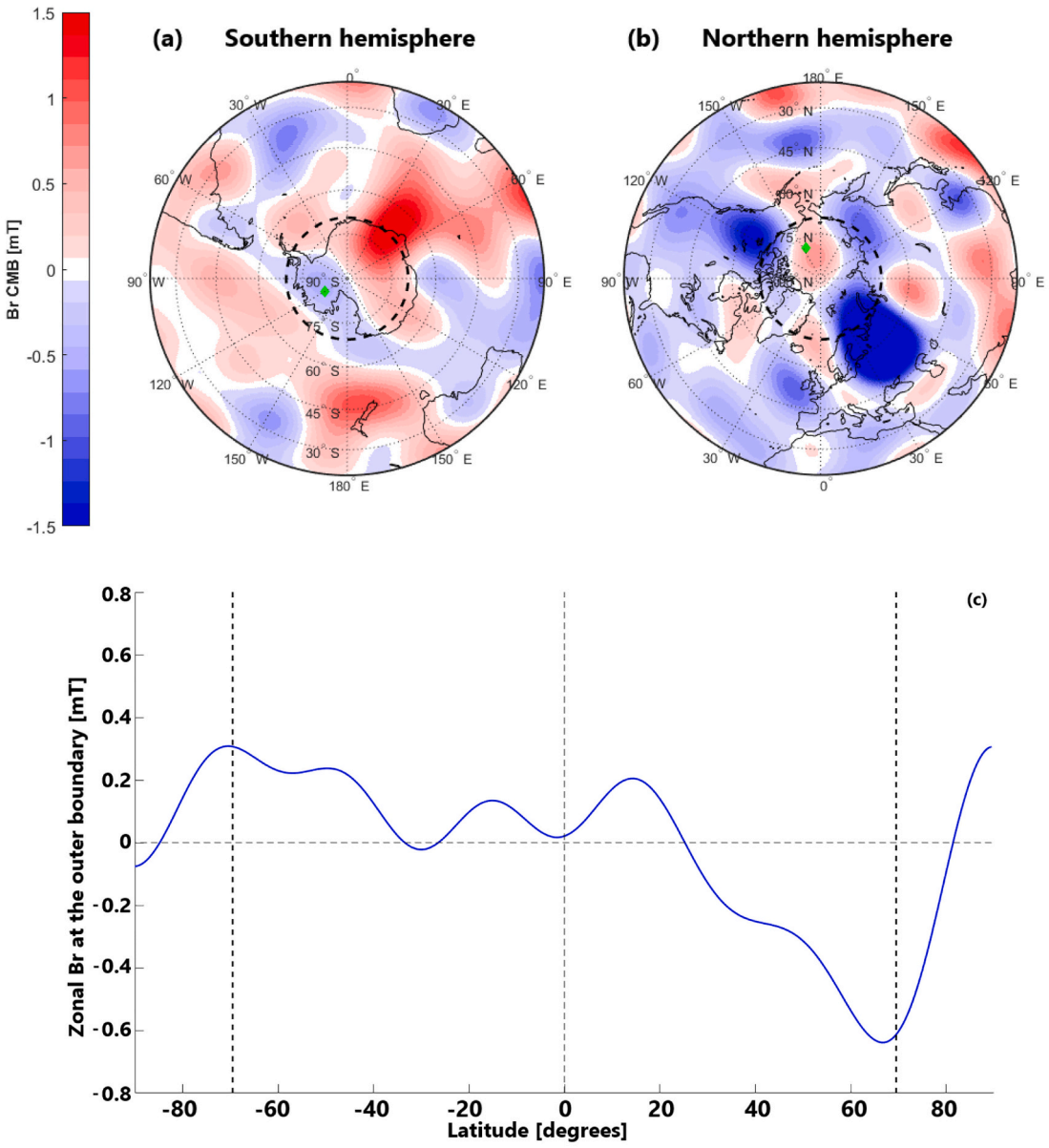

Fig. 9. South (a) and North (b) polar views of B_r on the outer boundary for a snapshot from case 12 of Terra-Nova et al. (2019). (c) Zonal radial field vs. latitude. The TC and equator are denoted by dashed vertical lines. This snapshot corresponds to a very strong northern polar minimum. Polar minima values for the northern hemisphere are $\frac{|dB_r^e|}{max|B_r^e|} = 1.48$; $\frac{|dB_r|}{max|B_r^e|} = 7.13$; $\frac{S_{TC}^{rev}}{S_{TC}} = 0.33$; $\lambda_{mean} = 79.84°$; $\lambda_{cm} = 78.68°$; $\phi_{cm} = -154.25°$. For the southern hemisphere $\frac{|dB_r^e|}{max|B_r^e|} = 0.60$; $\frac{|dB_r|}{max|B_r^e|} = 3.27$; $\frac{S_{TC}^{rev}}{S_{TC}} = 0.43$; $\lambda_{mean} = -81.34°$; $\lambda_{cm} = -81.38°$; $\phi_{cm} = -118.96°$.

according to (12) (Fig. 2a) and a very weak polar minimum according to (13) (Fig. 2b).

Fig. 4a shows the latitude of the center of mass of reversed flux inside the TC over the 1840–2020 period. In 1840, the latitude of the center of mass inside the northern TC was ∼74°. The reversed flux drifted towards the rotation axis until 1925, then it moved equatorward until 1975. Finally, its latitude remained roughly constant from thereafter. In the southern hemisphere, the latitude of the center of mass of reversed flux was roughly constant near the TC rim until 1920, then it drifted poleward and became almost steady at ∼80°. Due to the dominance of a single reversed flux in the southern hemisphere, the mean latitude of reversed flux (15) gives very similar results (Fig. 5). In the northern hemisphere, the reversed flux is sometimes fragmented although one patch is often larger and more intense than the others, hence Figs. 4a and 5 are practically identical for the northern TC as well.

Fig. 4b shows the longitude of the reversed flux center of mass (18). In 1840, the northern reversed flux center of mass was located at ∼70°W. It has drifted eastward to 60°E in 1930. Then it re-appeared in 70°W in 1940. Thereafter, it remained roughly constant until 2020. For the southern hemisphere, there was no reversed flux between 1845 and 1875 for the mean model. After 1875, the longitude of reversed flux slowly drifted from 20°E until 40°E in 2020. Overall, Fig. 4 provides additional evidence for strong temporal variability in the northern TC, especially concerning the longitude of reversed flux.

Next we explored the possible impact of the polar minima on the axial dipole and its temporal evolution. Fig. 6 shows polar views of the spatial contributions to the axial dipole $B_r cos(\theta)$(5) for the year 2010. For both hemispheres normal contributions are negative (in blue) and

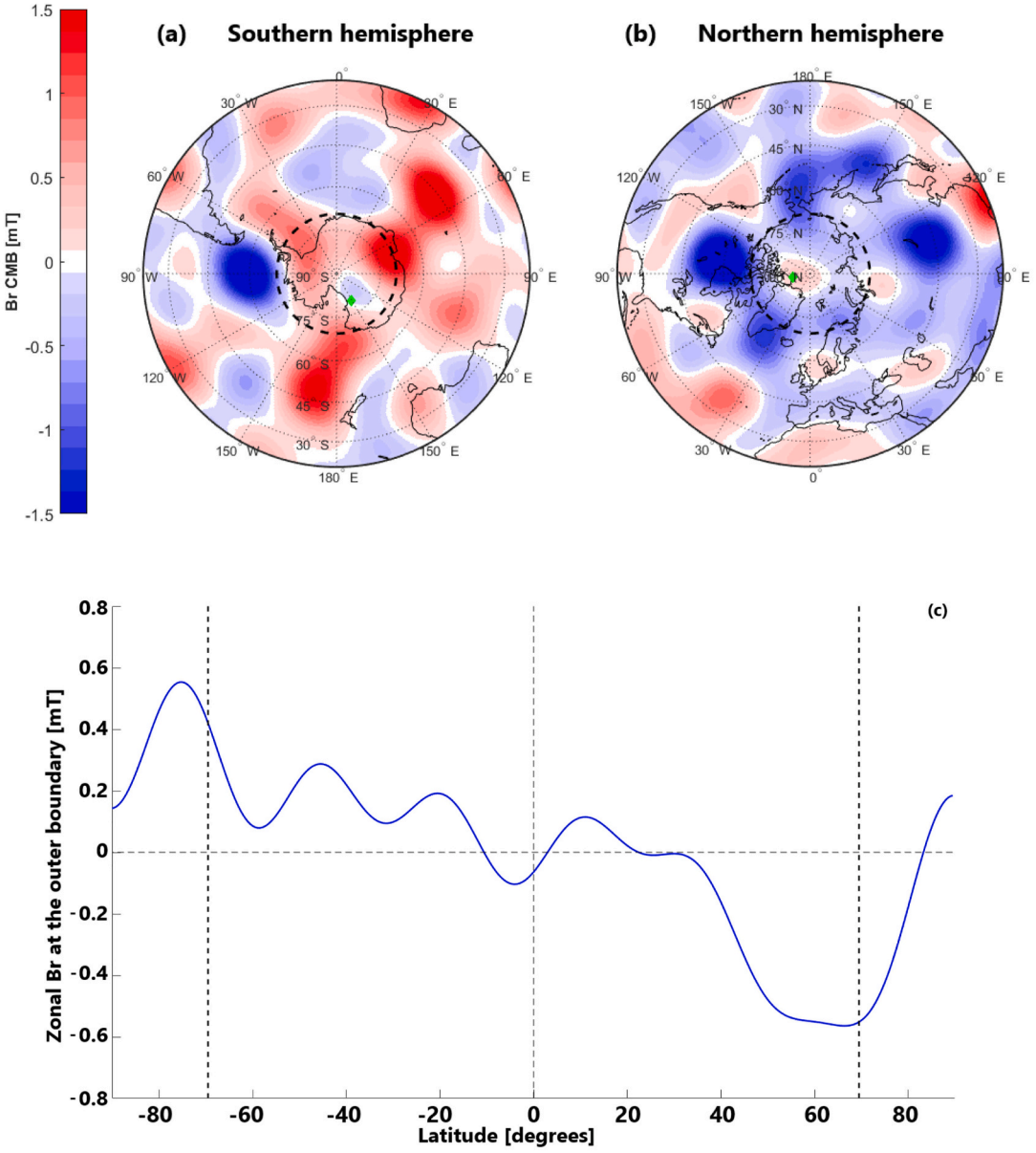

Fig. 10. As in Fig. 9 for another snapshot from dynamo model case 12. This snapshot corresponds to typical values of polar minima (12) and (13). Polar minima values for the northern hemisphere are $\frac{|dB_r^z|}{max|B_r^z|} = 1.33$; $\frac{|dB_r|}{max|B_r^z|} = 4.16$; $\frac{S_{TC}^{rev}}{S_{TC}} = 0.14$; $\lambda_{mean} = 84.74°$; $\lambda_{cm} = 83.93°$; $\phi_{cm} = -77.40°$. For the southern hemisphere $\frac{|dB_r^z|}{max|B_r^z|} = 0.73$; $\frac{|dB_r|}{max|B_r^z|} = 3.07$; $\frac{S_{TC}^{rev}}{S_{TC}} = 0.12$; $\lambda_{mean} = -79.61°$; $\lambda_{cm} = -79.66°$; $\phi_{cm} = 151.23°$.

reversed contributions are positive (in red). The strongest sources of axial dipole appear just outside the TC in the northern hemisphere and inside the TC in the southern. However, even in the southern hemisphere, the integrated contribution inside the TC is relatively weak simply because of its small area.

Fig. 7a presents the well-known historical decrease of the axial dipole moment (Gubbins, 1987; Olson and Amit, 2006; Finlay, 2008). The curves in Fig. 7b and c represent contributions from outside and inside the TC, respectively. Three of these four curves are roughly constant with time, while only the contribution outside the southern TC exhibits the same rate of decrease as the total. This is in agreement with previous studies that identified the origin of the axial dipole decrease in the southern hemisphere (Olson and Amit, 2006). Here we further identified the region outside the southern TC as the origin of the dipole decrease. It is related to the growth and intensification of the South Atlantic Anomaly (Terra-Nova et al., 2017), which is mainly dictated by the expansion and intensification of reversed flux at mid latitudes of the southern hemisphere (see the broad red structure in Fig. 6a).

4.2. Numerical dynamo models

Next we analyzed the dynamo models of Terra-Nova et al. (2019) with heterogeneous outer boundary heat flux inferred from a lower mantle seismic tomography model (Masters et al., 2000). Fig. 8a and b show timeseries of the polar minima magnitudes for a typical dynamo model (case 12, $E = 3{\cdot}10^{-4}, Ra = 5{\cdot}10^{6}, Pm = 4, q^{*} = 0.4$ and $Rm = 419$). There is a strong temporal variability for both hemispheres with large high frequency oscillations. However, at most times the northern polar minimum is significantly stronger than the southern. The mean values are 1.03/0.72 based on (12) and 3.58/2.82 based on (13) for the northern/southern hemisphere, respectively (Table 1), confirming this north/south dichotomy. Fig. 8c shows the relative surface of the

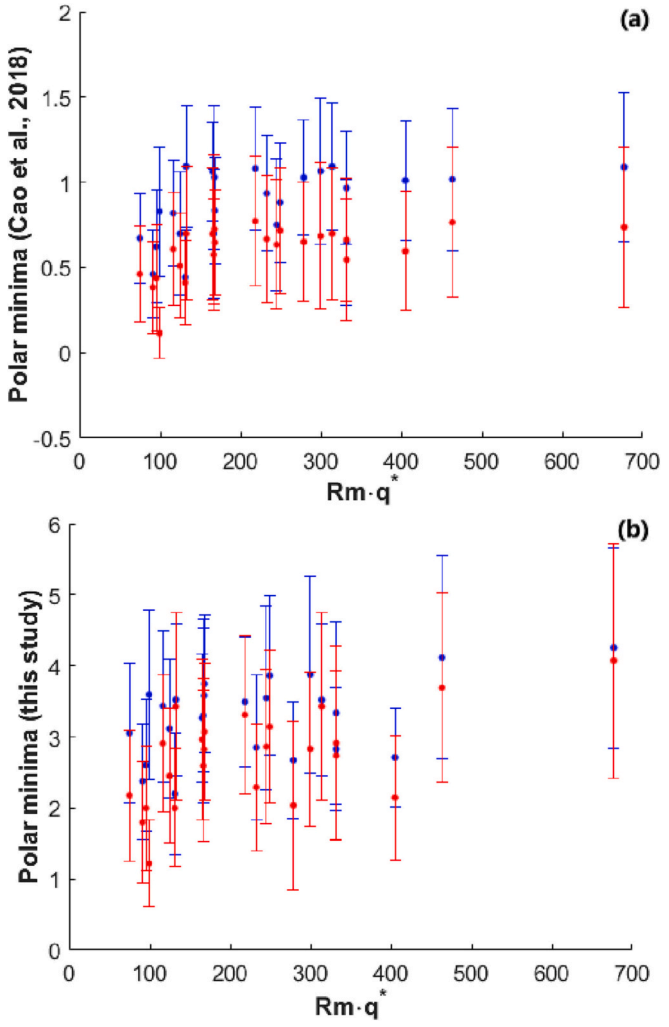

Fig. 11. Northern (blue) and southern (red) polar minima amplitudes based on (12) (a) and (13) (b) vs. $Rm{\cdot}q^*$. Error bars denote standard deviations which represent temporal variabilities. Each error bar corresponds to a separate dynamo model.

reversed flux inside the TC as a function of time for the same dynamo model. As in Fig. 8a and b, the amount of reversed flux exhibits high frequency oscillations. Nevertheless, at most times reversed flux covers a larger area inside the northern TC than inside the southern (Fig. 8c) with the mean relative surface area being $\sim 50\%$ larger in the northern hemisphere than in the southern (Table 1).

Figs. 9 and 10 show two selected snapshots of the dynamo model shown in Fig. 8. Fig. 9 shows a snapshot where the northern polar minimum is particularly strong. In the northern hemisphere, the area of reversed flux covers a third of the TC. There is a very large contrast between the field at the pole and the peak field at the TC edge, which leads to the very large polar minimum. In contrast, Fig. 10 shows a snapshot where the polar minima amplitudes are typical, i.e. close to their long-term average values, for this dynamo model. In the northern hemisphere, a single reversed flux patch is centered on the geographical pole and intense normal flux patches cluster near the edges of the TC. In the southern hemisphere, the morphology is similar but the reversed flux patch is off the pole and an additional strong reversed flux patch appears outside the TC. This snapshot resembles the geomagnetic field models both in the field morphology, especially at high latitudes, and in the magnitudes of polar minima, in particular the north/south dichotomy.

Table 1 presents the polar minima statistics for all the dynamo models. These quantifications are temporal averages of (12), (13), (14) and (18). The standard deviations correspond to the temporal variability, which is large due to the chaotic nature of the dynamo models. Almost all dynamo models show significant differences of polar minima amplitudes between the two hemispheres. The mean area of the reversed flux inside the northern TC is also larger than in the southern. The polar minima for both measures (12) and (13) and both hemispheres are shown as a function of $Rm{\cdot}q^*$ in Fig. 11. Here $Rm{\cdot}q^*$ was chosen as a run identifier (e.g. Davies and Constable, 2017) which combines global and boundary-driven properties. For both measures, the northern polar minimum is more intense than the southern (Fig. 11). Nevertheless, the large standard deviations mean that there are snapshots where the polar minima are larger in the southern hemisphere than in the northern (Fig. 11).

Next we analyzed the contributions to the axial dipole in the dynamo models. Fig. 12 shows timeseries of a typical axial dipole evolution. The total axial dipole intensity for the entire duration of the run contains several long episodes of dipole increase and decrease (Fig. 12a). We focus on a typical dipole decrease event in Fig. 12b. Fig. 12c and d show that the contributions to this dipole decrease event from outside the TC are larger than those from inside the TC for both hemispheres. However, note that the northern contribution is larger (Fig. 12c). Here the dipole decrease originates in both hemispheres (outside the TC).

Table 2 presents the temporal correlations between the polar minima magnitudes and the relative surface area of reversed flux in the TC for both the geomagnetic field and the dynamo models for both hemispheres. In the geomagnetic field, the correlation is low in the northern hemisphere and close to perfect in the southern. In the numerical dynamos, the correlations are positive and in most cases larger than 0.2, i.e statistically significant (Rau et al., 2000).

5. Discussion

We propose a new measure of polar minima based on (13). This measure relies on the peak intensity of high-latitude normal flux patches which better reflects the strength of fluid downwellings at the edge of the TC. A measure that relies on the peak zonal values of B_r(12) as proposed by Cao et al. (2018) gives smoother results and may introduce a bias to the estimated magnitudes of the polar minima. For the historical period, based on (12) the northern polar minimum is more intense than the southern at most times. This difference diminishes and the southern polar minimum becomes stronger at the end of the 20th century (Fig. 2a). In contrast, with the new measure (13), the northern polar minimum is more intense than the southern at all times (Fig. 2b), and overall the difference between the two hemispheres is larger based on the new measure than based on that of Cao et al. (2018). In summary, we conclude that the geomagnetic polar minima are significantly stronger in the northern hemisphere during the historical era.

The two hemispheres also behave differently in terms of the extent of the reversed flux inside the TC. Fig. 2c reveals a significantly larger reversed flux area in the northern TC than in the southern. Averaging over the historical era, the reversed flux covers 19% of the area inside the northern TC and only 7% of the area inside the southern (Table 1).

The mean latitude (15) and the latitude of the center of mass of the reversed flux (18) are extremely similar due to the morphology of the geomagnetic field inside the TC which is often dominated by a single reversed flux patch off the geographic pole. These results are in agreement with the single off-pole upwelling plume found in the dynamo models of Sreenivasan and Jones (2005). The results also conform with one of the alternative scenarios of Cao et al. (2018) in which large-scale non-axisymmetric and/or time-varying polar upwellings could induce strong polar minima.

We found stronger temporal variability inside the TC of the northern hemisphere than inside the southern e.g. in the area of reversed flux (Fig. 2c) and its center of mass longitude (Fig. 4b). The stronger variability in the northern hemisphere may point to north/south dichotomy

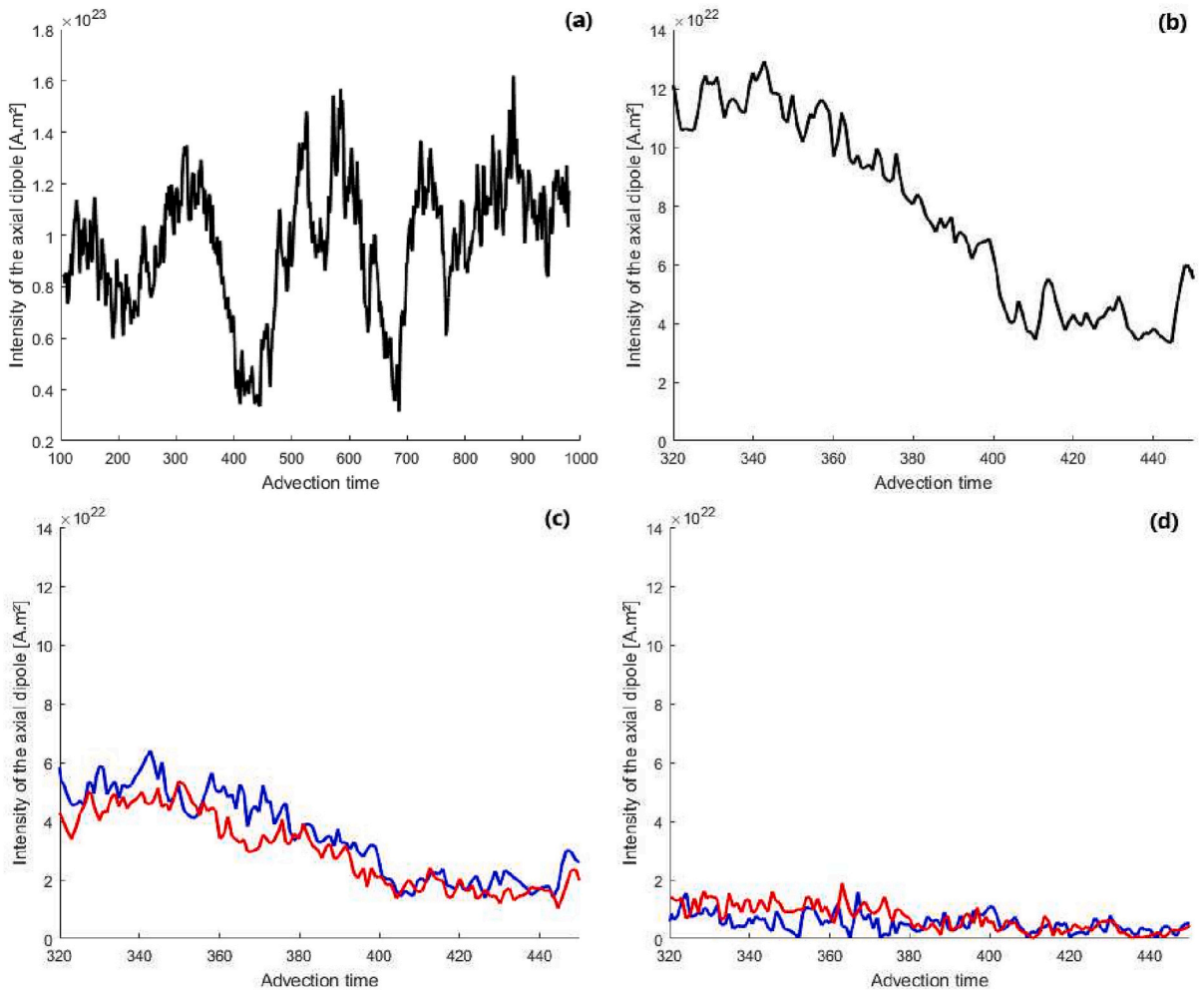

Fig. 12. Intensity of the axial dipole (in Am^2) for a dipole decrease event in numerical dynamo model case 12. (a) Total intensity of the dipole over the entire simulation. (b) Total intensity for a dipole decrease event. (c) Contributions from outside the TC during the dipole decrease event. (d) Contributions from inside the TC during the dipole decrease event. In (c) and (d) northern/southern hemispheres are denoted by blue/red lines, respectively.

in core flow activity. Olson and Aurnou (1999) also found different behavior between northern and southern TC dynamics with evidence for an anticyclone at the edge of the northern TC but not at the southern. Similarly, Livermore et al. (2017) inferred an accelerating high-latitude azimuthal jet in the northern hemisphere, but they could not detect such a jet in the southern hemisphere at the same latitude. They argued that the weak SV at high-latitudes of the southern hemisphere is due to a weak azimuthal field gradient so an equatorially symmetric southern azimuthal jet would produce weak SV due to field-flow alignment, hence such a jet cannot be disproved. The azimuthal field gradient is indeed stronger near the edge of the northern TC than in the southern, but the SV dichotomy is much larger (compare Figs. 1 and 4 of Livermore et al., 2017). Thus, the huge difference in the observed SV between the two hemispheres may require also a stronger flow at high latitudes of the northern hemisphere which may explain the stronger geomagnetic northern polar minimum. Indeed, the core flow model of Gillet et al. (2019) contains a significantly stronger zonal jet at high latitudes of the northern hemisphere than at high latitudes of the southern, in agreement with earlier inversions of geomagnetic SV (Pais and Hulot, 2000; Amit and Olson, 2006).

The historical geomagnetic field covers only 180 years of core dynamics. Because the advection time in the outer core is roughly 140 years (Terra-Nova and Amit, 2020), the historical era covers merely a bit more than one advection time. In order to explore in a more statistically meaningful way the characteristics of polar minima, dynamo models provide much longer timeseries. In addition, systematic studies of dynamo models may provide insight to the dependence of polar minima on physical processes in the core (Cao et al., 2018). Here we focus on the impact of the CMB heat flux heterogeneity on the polar minima.

All the investigated dynamo models (except one) show more intense polar minima in the northern hemisphere than in the southern based on both measures (12) and (13) (Fig. 11). This can be readily explained by the pattern of the outer boundary heat flux that was imposed on the dynamo simulations (Fig. 13). A larger heat flux at the south pole compared to the north pole results in a stronger mantle-driven polar downwelling that opposes the polar upwelling and reduces the field dispersion there. Therefore, the radial field at the south pole becomes less weak than at the north pole. In addition, the heat flux outside the TC is larger in the northern hemisphere than in the southern due to the southern centers of the two Large Low Shear-Wave Velocity Provinces below Africa and the Pacific. Thus, stronger mantle-driven downwellings in the northern hemisphere outside the TC induce a stronger peak B_r in the northern hemisphere. The dual effect of reducing the field dispersion in the south pole and enhancing the intense flux patches in the northern hemisphere leads to the mantle-driven dichotomy in the polar minima.

The striking hemispheric dichotomy in the dynamo models of Terra-Nova et al. (2019) is also evident in the flow patterns. In their Fig. 13c, polar upwellings prevail in both hemispheres, but the northern one is clearly larger and stronger. In addition, mid and high latitudes of the

Table 2
Temporal correlations C^z and C between the magnitudes of the polar minima (12) and (13) and relative areas of reversed flux inside the TC (14) for the northern/southern hemisphere.

Case	$C^z\left(\frac{\lvert dB_r^z\rvert}{max\lvert B_r^z\rvert}, \frac{S_{TC}^{rev}}{S_{TC}}\right)$		$C\left(\frac{\lvert dB_r\rvert_{max}}{\lvert B_r\rvert_{max}}, \frac{S_{TC}^{rev}}{S_{TC}}\right)$	
	North	South	North	South
Earth	0.1560	0.988	−0.124	0.927
2	0.427	0.449	0.189	0.237
3	0.376	0.357	0.087	0.286
4	0.403	0.373	0.075	0.223
5	0.385	0.311	0.146	0.239
6	0.425	0.337	0.369	0.259
7	0.339	0.292	0.279	0.357
8	0.392	0.369	0.315	0.279
9	0.455	0.079	0.487	0.028
10	0.329	0.299	0.232	0.279
11	0.268	0.278	0.302	0.213
12	0.394	0.397	0.299	0.403
13	0.439	0.213	0.291	0.197
15	0.380	0.451	0.200	0.248
16	0.480	0.383	0.281	0.214
17	0.427	0.433	0.367	0.232
18	0.377	0.381	0.343	0.254
19	0.391	0.368	0.316	0.279
20	0.469	0.512	0.341	0.312
21	0.407	0.409	0.309	0.323
22	0.535	0.478	0.480	0.333
23	0.557	0.318	0.502	0.313
26	0.299	0.314	0.244	0.155
27	0.240	0.277	0.259	0.230
28	0.402	0.418	0.100	0.329

northern hemisphere are dominated by downwellings, whereas upwellings dominate the southern mid and high latitudes, especially below the South Atlantic. This north/south dichotomy in the long-term time-average flow induces the stronger northern polar minimum in the dynamo models.

We attempted to fit scaling laws which may reveal the dependence of the polar minima on physical processes. These fits are in general poor (not shown). This suggests some non-monotonic dependence of the polar minima amplitudes on the dynamo control parameters, in particular q^*. Indeed, some pairs of dynamo models with identical control parameters except q^* favor northern polar minima, e.g. cases 3 and 4, whereas cases 7 and 8 favor southern polar minima. Sahoo and Sreenivasan (2020) used numerical dynamos with tomographic outer boundary heat flux to explain the relative strengths and coherences of the normal geomagnetic flux patches beneath Canada and Siberia. According to the tomographic model they used, the heat flux is larger under Canada, but counter-intuitively the observed geomagnetic field below Siberia is more intense and stable. In their dynamo models, at moderate convection vigor the Canadian patch was indeed more intense and stable than the Siberian patch. But for increasing Ra, the Canadian patch split and became more unstable due to more turbulent local conditions, while the Siberian patch remained intense and stable. This is an example of a non-monotonic behavior of field features as a function of the dynamo control parameters. If this is indeed the case, scaling laws might not be applicable for our purposes.

The origin of the geomagnetic dipole decrease is an outstanding question in core dynamics. Olson and Amit (2006) established that the dipole decrease (Fig. 7a) originates in the southern hemisphere. We further found that this decrease originates outside the southern TC (Fig. 7b) where the growth of reversed flux patches (Fig. 6a) below the South Atlantic is related to weak surface intensity there, i.e. the South Atlantic Anomaly (Bloxham et al., 1989; Terra-Nova et al., 2017; Amit et al., 2021). In the dynamo models, the northern contribution to the axial dipole is larger than the southern, as in the geomagnetic field. In addition, the dipole decrease events in the dynamo models are controlled by the field outside the TC, again as in the geomagnetic field. However, in the dynamo models both hemispheres contribute to the dipole decrease substantially, whereas in the geomagnetic field the decrease originates only in the southern hemisphere.

The intensity of the geomagnetic polar minima and the surface of reversed flux inside the TC show almost no correlation for the northern hemisphere and an almost perfect correlation for the southern hemisphere (Table 2). In the southern hemisphere, the emergence and increase of the polar minimum is accompanied by an increase in the area of reversed flux inside the TC (Fig. 2c). In contrast, in the northern hemisphere, the polar minimum is at some periods strong due to the presence of a weak normal field inside the TC, which decreases the correlation.

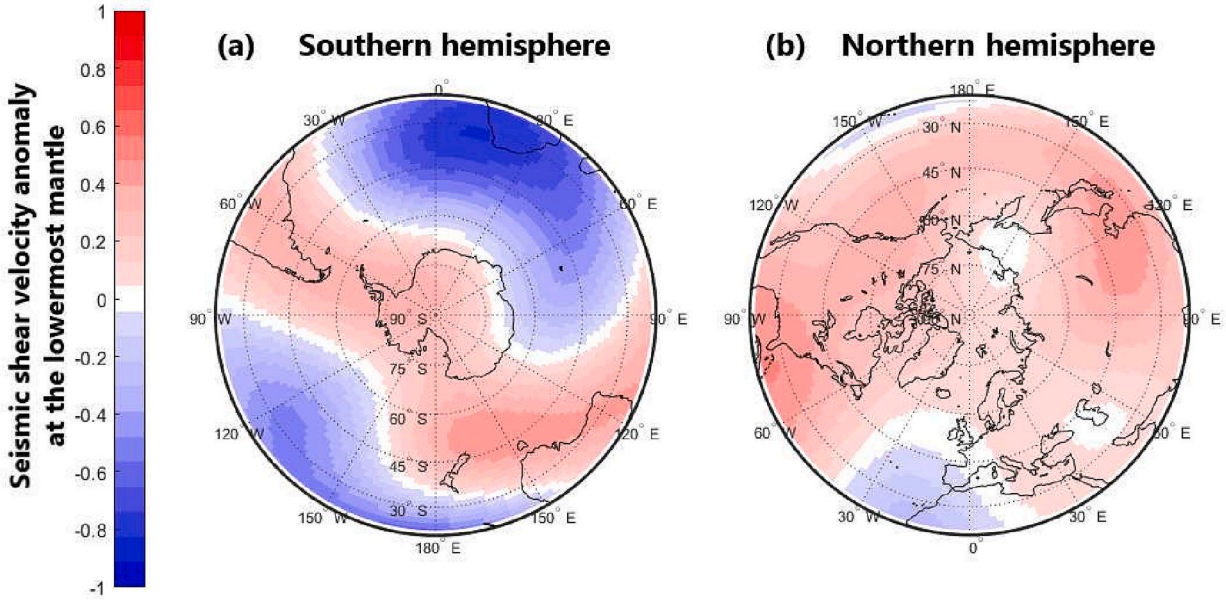

Fig. 13. Non-dimensional seismic shear-wave velocity anomaly at the lowermost mantle based on the tomographic model of Masters et al. (2000) truncated at spherical harmonic degree and order 6. This pattern was imposed as a heterogeneous outer boundary heat flux in the dynamo models. Red/blue corresponds to positive/negative heat flux anomaly, respectively.

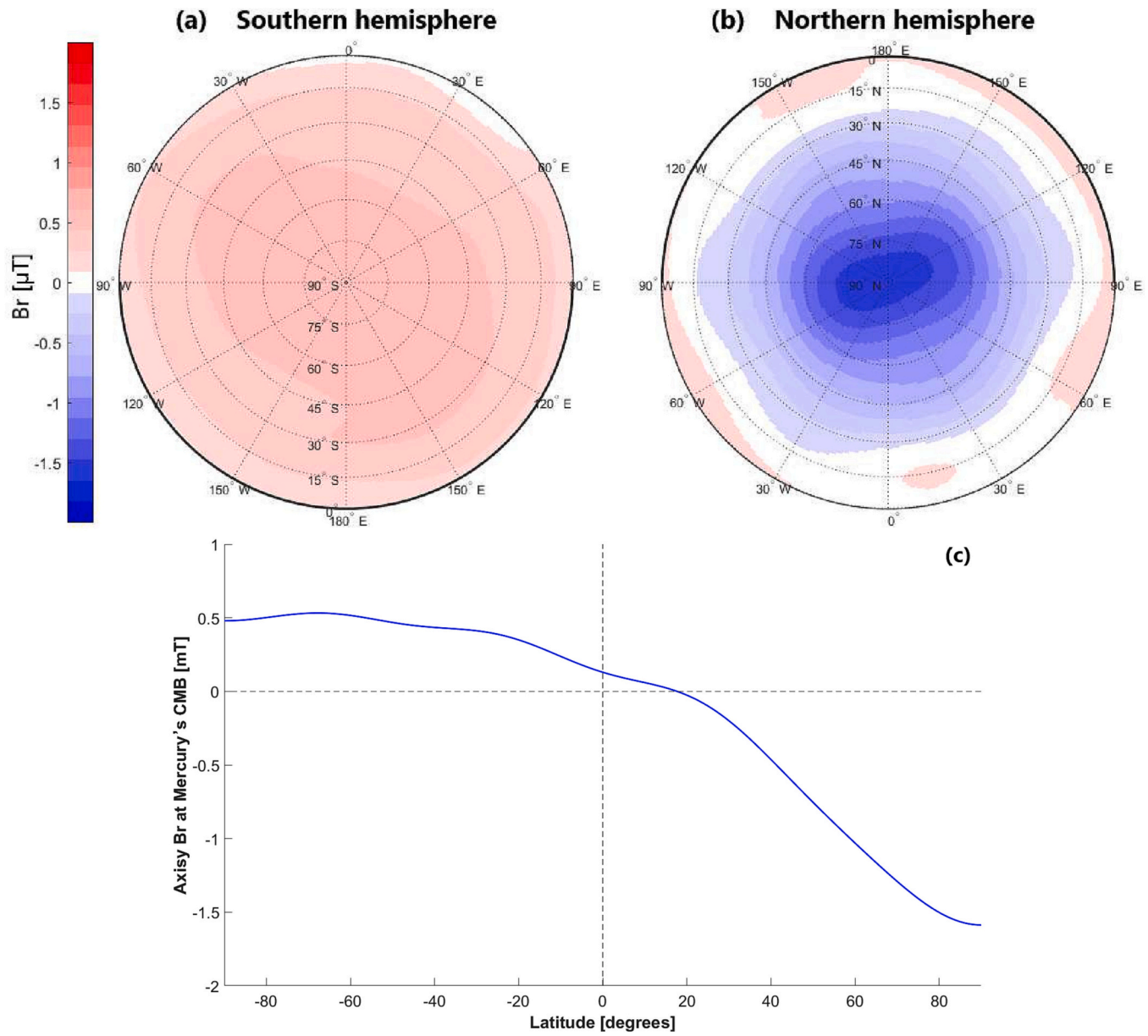

Fig. 14. South (a) and North (b) polar views of B_r on the CMB of Mercury based on the model of Wardinski et al. (2021). (c) Zonal radial field vs. latitude. In (c) the equator is denoted by a dashed vertical line.

Can polar minima be observed for magnetic fields of other planets? The magnetic field of Mercury is very large scale and highly axisymmetric (Anderson et al., 2011; Oliveira et al., 2015; Thébault et al., 2018). A careful analysis of the MESSENGER data allowed the construction of internal field models with non-zonal spherical harmonic coefficients (Wardinski et al., 2021). Fig. 14 reveals some weak non-axisymmetric features (e.g. the elliptical B_r contours around the north pole). Note that inferences upon the southern polar minimum of Mercury are less robust because any magnetic field model of Mercury relies on data exclusively over the northern hemisphere due to the highly eccentric orbit of the MESSENGER mission. Due to the non-zonal terms, some non-zero values for the polar minima at both hemispheres are obtained, though the values are very small (Table 1). The absence of substantial polar minima at Mercury's field is likely due to the presence of a thick stratified layer at the top of the core (Christensen, 2006) that diffuses small-scale field features such as the polar minima (Olson et al., 2017). In contrast, the magnetic field of Jupiter (Sharan et al., 2022) exhibits significantly stronger polar minima than Earth's (Table 1). Fig. 15b shows intense northern mid- and high-latitude normal flux patches and reversed flux patches near the north pole. The field morphology in the southern hemisphere (Fig. 15a) is very different, with an isolated intense normal flux patch near the equator and mild field elsewhere. The resulting polar minima are strong, especially in the northern hemisphere. However, caution is required in inferring TC dynamics in Jupiter's interior from the Jovian magnetic polar minima because the axial invariance of the flow outside the TC (2) and the thermal wind inside the TC (4) both rely on assuming incompressible flow which does not hold for gas giants. The magnetic polar minima on Earth and Jupiter might therefore have distinctive dynamical origins.

In summary, geomagnetic field models indicate that the polar minima are more intense in the northern hemisphere than in the southern, but this feature might be transient because the historical period is somewhat short. Numerical dynamo models with tomographic outer boundary heat flux also exhibit more intense polar minima in the northern hemisphere than in the southern, but due to computational limitations the control parameters in these models are far from Earth-

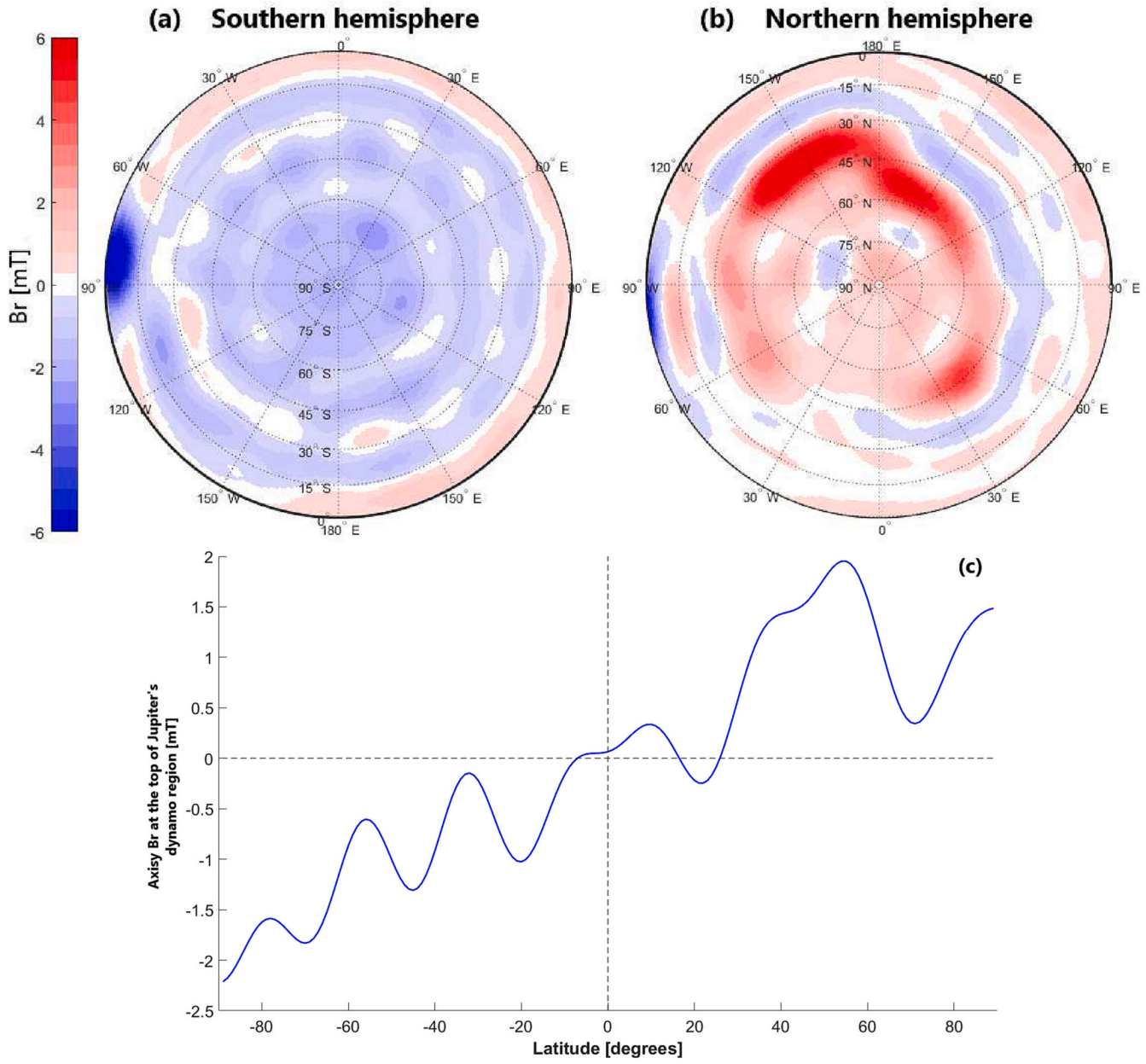

Fig. 15. South (a) and North (b) polar views of B_r at the top of the dynamo region of Jupiter based on the model of Sharan et al. (2022). (c) Zonal radial field vs. latitude. In (c) the equator is denoted by a dashed vertical line.

like values hence caution should be taken in the interpretations of these models. Together, however, these two results make a compelling case for a mantle-driven north/south dichotomy of TC dynamics and geomagnetic polar minima.

Author contributions statement

Maxime Lézin: Data curation, Formal analysis, Investigation, Methodology, Software, Validation, Visualization, Writing - original draft, Writing - review & editing. Hagay Amit: Conceptualization, Formal analysis, Investigation, Methodology, Project administration, Supervision, Validation, Writing - review & editing. Filipe Terra-Nova: Conceptualization, Investigation, Validation, Writing - review & editing. Ingo Wardinski: Conceptualization, Investigation, Validation, Writing - review & editing.

Declaration of Competing Interest

The authors declare that they have no known competing financial interests or personal relationships that could have appeared to influence the work reported in this paper.

Data availability

Data will be made available on request.

Acknowledgements

We thank Shivangi Sharan for providing the Jovian magnetic field model. F.T.-N. was supported by the Centre national d'études spatiales (CNES). We thank Phil Livermore and an anonymous reviewer for their constructive comments.

Appendix A. Additional geomagnetic polar minima visualizations

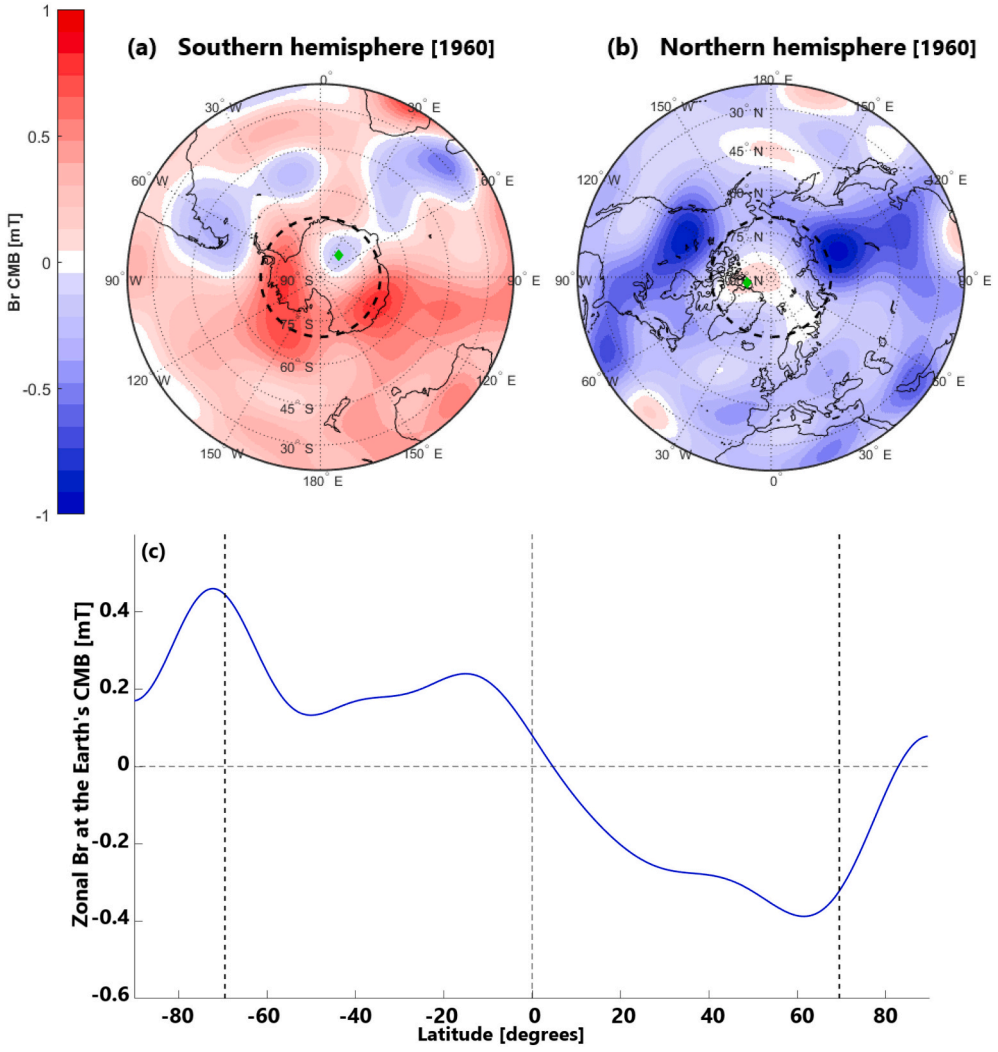

Fig. A1. As in Fig. 3 for the year 1960. Polar minima values for the northern hemisphere are $\frac{|dB_r^z|}{max|B_r^z|} = 1.01$; $\frac{|dB_r|}{max|B_r^z|} = 2.25$; $\frac{S_{TC}^{rev}}{S_{TC}} = 23.25\%$; $\lambda_{mean} = 82.78°$; $\lambda_{cm} = 81.69°$; $\phi_{cm} = -76.17°$. For the southern hemisphere $\frac{|dB_r^z|}{max|B_r^z|} = 0.63$; $\frac{|dB_r|}{max|B_r^z|} = 1.36$; $\frac{S_{TC}^{rev}}{S_{TC}} = 13.45\%$; $\lambda_{mean} = -80.17°$; $\lambda_{cm} = -80.19°$; $\phi_{cm} = 40.67°$.

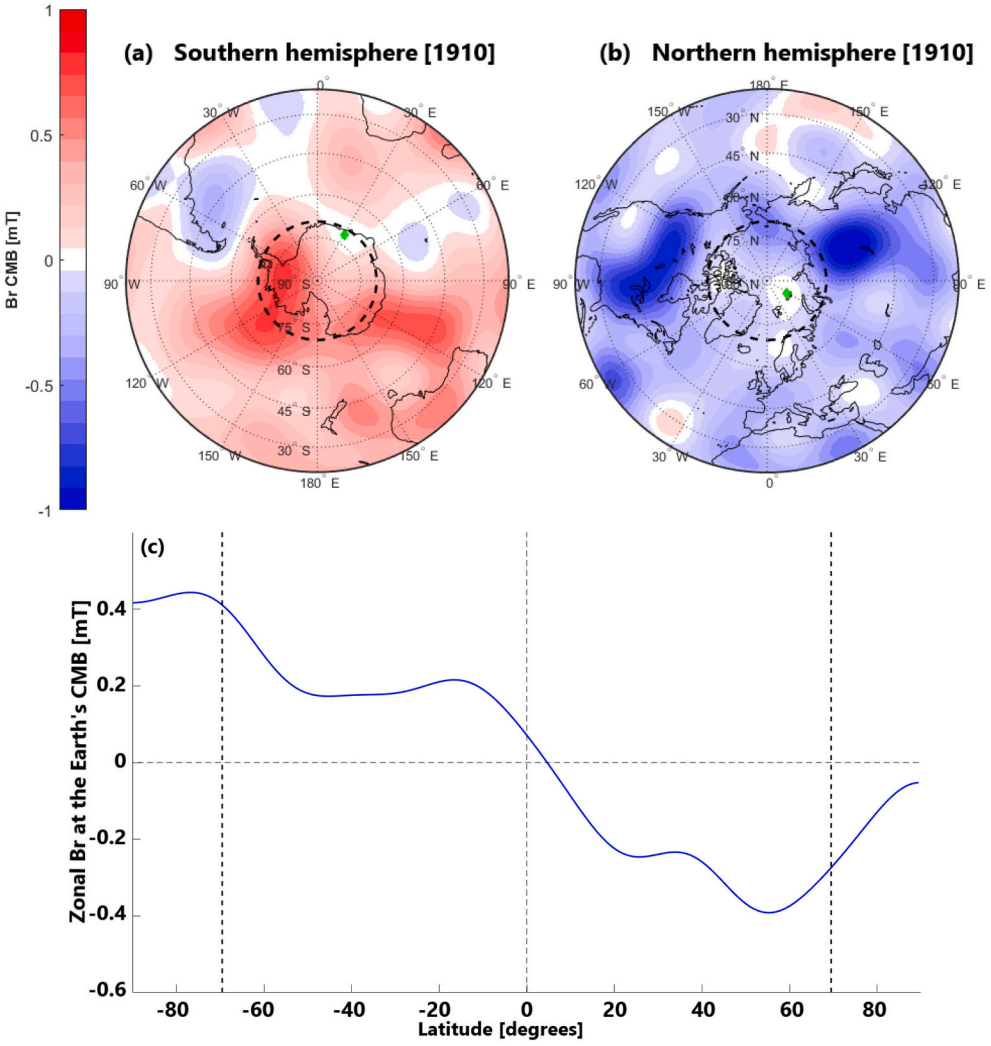

Fig. A2. As in Fig. 3 for the year 1910. Polar minima values for the northern hemisphere are $\frac{|dB_r^e|}{max|B_r^e|} = 0.77$; $\frac{|dB_r|}{max|B_r^e|} = 2.38$; $\frac{S_{TC}^{rev}}{S_{TC}} = 3.29\%$; $\lambda_{mean} = 82.21°$; $\lambda_{cm} = 82.06°$; $\phi_{cm} = 56.77°$. For the southern hemisphere $\frac{|dB_r^e|}{max|B_r^e|} = 0.06$; $\frac{|dB_r|}{max|B_r^e|} = 0.81$; $\frac{S_{TC}^{rev}}{S_{TC}} = 0.80\%$; $\lambda_{mean} = -71.62°$; $\lambda_{cm} = -71.63°$; $\phi_{cm} = 31.04°$.

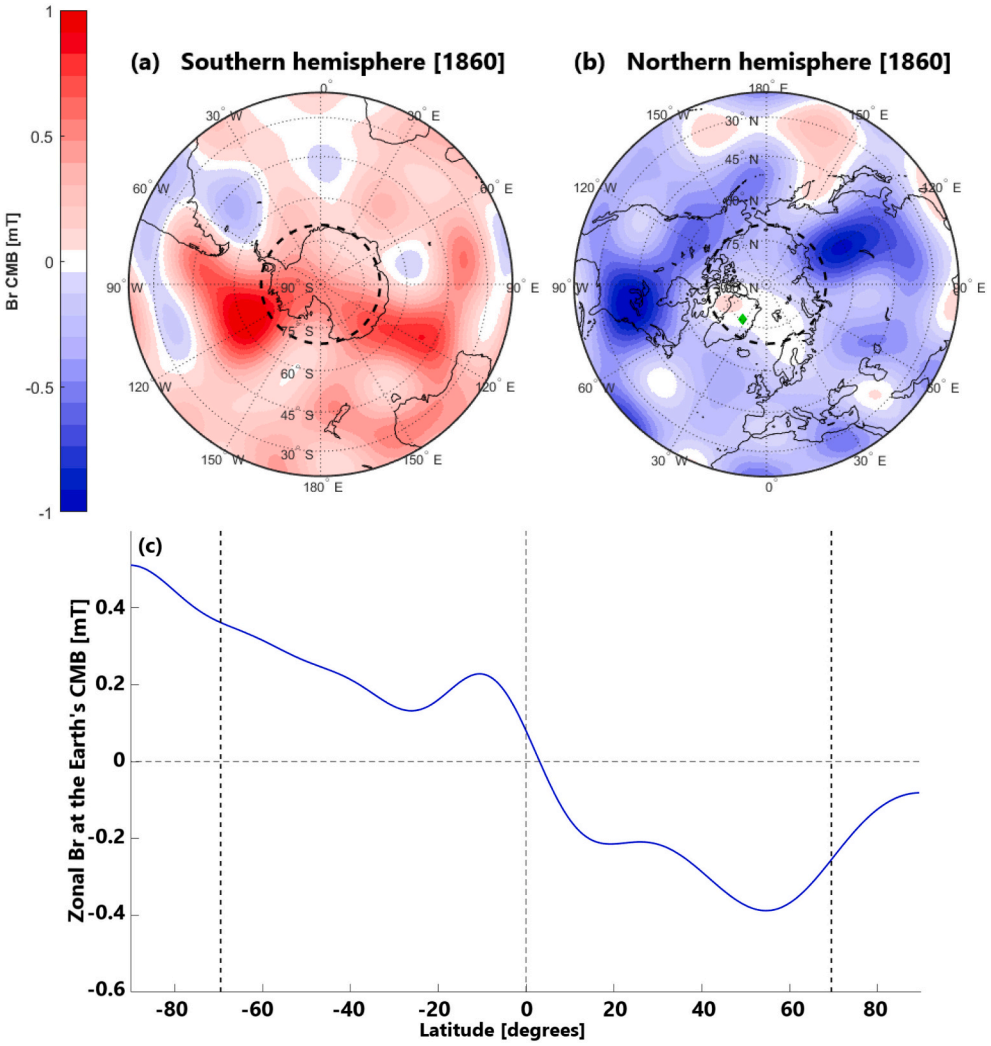

Fig. A3. As in Fig. 3 for the year 1860. Polar minima values for the northern hemisphere are $\frac{|dB_r^z|}{max|B_r^z|} = 0.60$; $\frac{|dB_r|}{max|B_r^z|} = 1.78$; $\frac{S_{TC}^{rev}}{S_{TC}} = 23.03\%$; $\lambda_{mean} = 75.93°$; $\lambda_{cm} = 75.56°$; $\phi_{cm} = -34.83°$. For the southern hemisphere $\frac{|dB_r^z|}{max|B_r^z|} = 0$; $\frac{|dB_r|}{max|B_r^z|} = 1.06$; $\frac{S_{TC}^{rev}}{S_{TC}} = 0$. For the southern hemisphere, $\lambda_{mean}, \lambda_{cm}$ and ϕ_{cm} are irrelevant because there is no reversed flux in the southern TC in 1860.

References

Amit, H., 2014. Can downwelling at the top of the Earth's core be detected in the geomagnetic secular variation? Phys. Earth Planet. Int. 229, 110–121.

Amit, H., Christensen, U.R., Langlais, B., 2011. The influence of degree-1 mantle heterogeneity on the past dynamo of Mars. Phys. Earth Planet. Int. 189 (1), 63–79.

Amit, H., Olson, P., 2006. Time-average and time-dependent parts of core flow. Phys. Earth Planet. Int. 155 (1), 120–139.

Amit, H., Olson, P., 2008. Geomagnetic dipole tilt changes induced by core flow. Phys. Earth Planet. Int. 166, 226–238.

Amit, H., Terra-Nova, F., Lézin, M., Trindade, R.I., 2021. Non-monotonic growth and motion of the South Atlantic Anomaly. Earth Planet Space 73 (38).

Anderson, B., Johnson, C., Purucker, M., Winslow, R., Slavin, J., Solomon, S., McNutt, R., Raines, J., Zurbuchen, T., 2011. The global magnetic field of Mercury from MESSENGER orbital observations. Science 333, 1859–1862.

Aubert, J., Amit, H., Hulot, G., Olson, P., 2008. Thermochemical flows couple the Earth's inner core growth to mantle heterogeneity. Nature 465, 758–761.

Aubert, J., Finlay, C.C., Fournier, A., 2013. Bottom-up control of geomagnetic secular variation by the Earth's inner core. Nature 502 (7470), 219–223.

Aurnou, J., Andreadis, S., Zhu, L., Olson, P., 2003. Experiments on convection in Earth's core tangent cylinder. Earth Planet. Sci. Lett. 212 (1–2), 119–134.

Biggin, A., Piispa, E., Pesonen, L., Holme, R., Paterson, G.A., Veikkolainen, T., Tauxe, L., 2015. Palaeomagnetic field intensity variations suggest Mesoproterozoic inner-core nucleation. Nature 526, 245–248.

Bloxham, J., Gubbins, D., Jackson, A., 1989. Geomagnetic secular variation. Phil. Trans. R Soc London. Ser. A, Math. Phys. Sci. 329, 415–502.

Buffett, B., 2014. Geomagnetic fluctuations reveal stable stratification at the top of the Earth's core. Nature 507, 484–487.

Busse, F.H., 1975. A model of the geodynamo. Geophys. J. Int. 42, 437–459.

Cao, H., Yadav, R.K., Aurnou, J.M., 2018. Geomagnetic polar minima do not arise from steady meridional circulation. Proc. Natl. Acad. Sci. 115 (44), 11186–11191.

Chandrasekhar, S., 2013. Hydrodynamic and hydromagnetic stability. Courier Corporation.

Christensen, U., Olson, P., Glatzmaier, G.A., 1998. A dynamo model interpretation of geomagnetic field structures. Geophys. Res. Lett. 25 (10), 1565–1568.

Christensen, U., Wicht, J., 2015. 8.10 - Numerical Dynamo Simulations. In: Schubert, G. (Ed.), Treatise on Geophysics (Second Edition). Elsevier, pp. 245–277.

Christensen, U.R., 2006. A deep dynamo generating Mercury's magnetic field. Nature 444, 1056–1058.

Christensen, U.R., Aubert, J., Hulot, G., 2010. Conditions for Earth-like geodynamo models. Earth Planet. Sci. Lett. 296 (3), 487–496.

Cormier, V.F., Bergman, M.I., Olson, P.L., 2021. Earth's Core: Geophysics of a Planet's Deepest Interior. Elsevier.

Cowling, T.G., 1934. The magnetic field of sunspots. Mon. Not. Roy. Astron. Soc. 94, 39–48.

Davies, C., Constable, C., 2017. Geomagnetic spikes on the core-mantle boundary. Nat. Commun. 8 (1), 1–11.

Finlay, C., Aubert, J., Gillet, N., 2016. Gyre-driven decay of the Earth's magnetic dipole. Nat. Commun. 7, 10422.

Finlay, C.C., 2008. Historical variation of the geomagnetic axial dipole. Phys. Earth Planet. Int. 170 (1–2), 1–14.

Gastine, T., Aubert, J., Fournier, A., 2020. Dynamo-based limit to the extent of a stable layer atop Earth's core. Geophys. J. Int. 222 (2), 1433–1448.

Gillet, N., Barrois, O., Finlay, C., 2015. Stochastic forecasting of the geomagnetic field from the COV-OBS.x1 geomagnetic field model, and candidate models for IGRF-12. Earth Planet Space 67 (71).
Gillet, N., Huder, L., Aubert, J., 2019. A reduced stochastic model of core surface dynamics based on geodynamo simulations. Geophys. J. Int. 219, 539–552.
Gillet, N., Schaeffer, N., Jault, D., 2011. Rationale and geophysical evidence for quasi-geostrophic rapid dynamics within the Earth's outer core. Phys. Earth Planet. Int. 187 (3), 380–390. Special Issue: Planetary Magnetism, Dynamo and Dynamics.
Glatzmaier, G.A., Roberts, P.H., 1996. Rotation and Magnetism of Earth's Inner Core. Science 274, 1887–1991.
Gubbins, D., 1987. Mechanism for geomagnetic polarity reversals. Nature 326 (6109), 167–169.
Gubbins, D., Bloxham, J., 1987. Morphology of the geomagnetic field and implications for the geodynamo. Nature 325, 509–511.
Gubbins, D., Jones, A.L., Finlay, C.C., 2006. Fall in Earth's magnetic field is erratic. Science 312 (5775), 900–902.
Gubbins, D., Willis, A.P., Sreenivasan, B., 2007. Correlation of Earth's Magnetic Field with Lower Mantle Thermal and Seismic Structure. Phys. Earth Planet. Int. 162 (3), 256–260.
Holme, R., 2015. Large-scale flow in the core. In: Olson, P. (Ed.), Treatise on Geophysics, second ed., vol. 8. Elsevier Science.
Holme, R., Olsen, N., 2006. Core surface flow modelling from high-resolution secular variation. Geophys. J. Int. 166 (2), 518–528.
Hulot, G., Eymin, C., Langlais, B., Mandea, M., Olsen, N., 2002. Small-scale structure of the geodynamo inferred from Oersted and Magsat satellite data. Nature 416, 620–623.
Jackson, A., Jonkers, A.R.T., Walker, M.R., 2000. Four centuries of geomagnetic secular variation from historical records. Philos. Trans.R. Soc. Lond. Ser. A 358, 957–990.
Jones, C.A., 2007. Thermal and Compositional Convection in the Outer Core. In: Treatise on Geophysics, first ed., vol. 8. Elsevier Science.
Kaneshima, S., Matsuzawa, T., 2015. Stratification of earth's outermost core inferred from SmKS array data. Prog. Earth Planet. Sci. 2 (1), 1–15.
Livermore, P.W., Hollerbach, R., Finlay, C.C., 2017. An accelerating high-latitude jet in Earth's core. Nat. Geosci. ISSN: 1752-0894 10 (1), 62–68.
Masters, G., Laske, G., Bolton, H., Dziewonski, A., 2000. The relative behavior of shear velocity, bulk sound speed, and compressional velocity in the mantle: Implications for chemical and thermal structure. Geophys. Monogr. Ser. 117, 63–87. AGU, Washington, D.C.
Metman, M.C., Livermore, P.W., Mound, J.E., 2018. The reversed and normal flux contributions to axial dipole decay for 1880–2015. Phys. Earth Planet. Int. 276, 106–117.
Moffatt, H.K., 1978. Field generation in electrically conducting fluids. Cambridge University Press, Cambridge, London, New York, Melbourne 2, 1–5.
Mound, J., Davies, C., Rost, S., Aurnou, J., 2019. Regional stratification at the top of Earth's core due to core–mantle boundary heat flux variations. Nat. Geosci. 12 (7), 575–580.
Oliveira, J.S., Langlais, B., Pais, M.A., Amit, H., 2015. A modified Equivalent Source Dipole method to model partially distributed mag- netic field measurements, with application to Mercury. J. Geophys. Res.: Planets 120, 1075–1094.
Olson, P., Amit, H., 2006. Changes in earth's dipole. Naturwissenschaften 93 (11), 519–542.
Olson, P., Aurnou, J., 1999. A polar vortex in the Earth's core. Nature 402, 170–173.
Olson, P., Christensen, U., Glatzmaier, G.A., 1999. Numerical modeling of the geodynamo: mechanisms of field generation and equilibration. J. Geophys. Res.: Solid Earth 104 (B5), 10383–10404.
Olson, P., Christensen, U.R., 2002. The time-averaged magnetic field in numerical dynamos with non-uniform boundary heat flow. Geophys. J. Int. 151 (3), 809–823.
Olson, P., Landeau, M., Reynolds, E., 2017. Dynamo tests for stratification below the core-mantle boundary. Phys. Earth Planet. Int. 271, 1–18.
Pais, A., Hulot, G., 2000. Length of day decade variations, torsional oscillations and inner core superrotation: evidence from recovered core surface zonal flows. Phys. Earth Planet. Int. 118 (3–4), 291–316.
Pais, M., Jault, D., 2008. Quasi-geostrophic flows responsible for the secular variation of the Earth's magnetic field. Geophys. J. Int. 173, 421–443.
Pedlosky, J., 1987. Geophysical Fluid Dynamics, second edition. Springer.
Rau, S., Christensen, U., Jackson, A., Wicht, J., 2000. Core flow inversion tested with numerical dynamo models. Geophys. J. Int. 141, 485–497.
Sahoo, S., Sreenivasan, B., 2020. Response of Earth's magnetic field to large lower mantle heterogeneity. Earth Planet. Sci. Lett. 549, 116507.
Schwaiger, T., Gastine, T., Aubert, J., 2019. Force balance in numerical geodynamo simulations: a systematic study. Geophys. J. Int. 219, S101–S114.
Sharan, S., Langlais, B., Amit, H., Thébault, E., Pinceloup, M., Verhoeven, O., 2022. The internal structure and dynamics of Jupiter unveiled by a high resolution magnetic field and secular variation model. Geophys. Res. Lett. 49, e2022GL098839.
Soderlund, K.M., King, E.M., Aurnou, J.M., 2012. The influence of magnetic fields in planetary dynamo models. Earth Planet. Sci. Lett. 333–334, 9–20.
Song, X., Richards, P.G., 1996. Seismological evidence for differential rotation of the Earth's inner core. Nature 382 (6588), 221–224.
Sreenivasan, B., Jones, C.A., 2005. Structure and dynamics of the polar vortex in the Earth's core. Geophys. Res. Lett. 32, L20301.
Taylor, G., 1917. Motion of solids in fluids when the flow is not irrotational. Proc. Roy. Soc. 93 (648), 99–113.
Terra-Nova, F., Amit, H., 2020. Magnetic boundary layers in numerical dynamos with heterogeneous outer boundary heat flux. Phys. Earth Planet. Int. 309, 106589.
Terra-Nova, F., Amit, H., Choblet, G., 2019. Preferred locations of weak surface field in numerical dynamos with heterogeneous core–mantle boundary heat flux: consequences for the South Atlantic Anomaly. Geophys. J. Int. 217, 1179–1199.
Terra-Nova, F., Amit, H., Hartmann, G.A., Trindade, R.I., 2015. The time dependence of reversed archeomagnetic flux patches. J. Geophys. Res. 120, 691–704.
Terra-Nova, F., Amit, H., Hartmann, G.A., Trindade, R.I., Pinheiro, K.J., 2017. Relating the South Atlantic Anomaly and geomagnetic flux patches. Phys. Earth Planet. Int. 266, 39–53.
Thébault, E., Langlais, B., Oliveira, J., Amit, H., Leclercq, L., 2018. A time-averaged regional model of the Hermean magnetic field. Phys. Earth Planet. Int. 276, 93–105.
Wardinski, I., Amit, H., Langlais, B., Thébault, E., 2021. The internal structure of Mercury's core inferred from magnetic observations. J. Geophys. Res.: Planets 126, e2020JE006792.